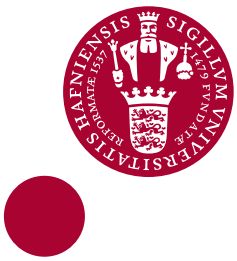

# A Functional Link between Nuclear RNA Decay and Transcriptional Control Mediated by the Polycomb Repressive Complex 2

Garland, William; Comet, Itys; Wu, Mengjun; Radzisheuskaya, Aliaksandra; Rib, Leonor; Vitting-Seerup, Kristoffer; Lloret-Llinares, Marta; Sandelin, Albin; Helin, Kristian; Jensen, Torben Heick

*Published in:*
Cell Reports

*DOI:*
10.1016/j.celrep.2019.10.011

*Publication date:*
2019

*Document version*
Publisher's PDF, also known as Version of record

Report

Cell Reports

# A Functional Link between Nuclear RNA Decay and Transcriptional Control Mediated by the Polycomb Repressive Complex 2

## Graphical Abstract

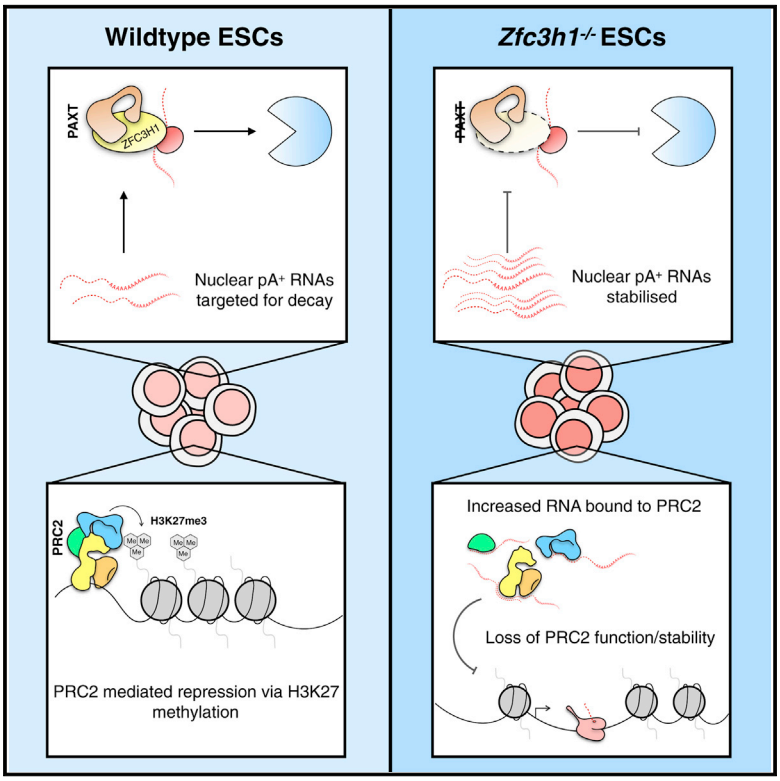


## Highlights

- Depletion of ZFC3H1 in mouse ESCs results in differentiation defects
- PRC2 target genes are deregulated in *Zfc3h1*$^{-/-}$ cells
- Chromatin binding of PRC2 and H3K27me3 is reduced in *Zfc3h1*$^{-/-}$ cells
- Increased binding of RNA impairs PRC2 complex stability

## Authors

William Garland, Itys Comet, Mengjun Wu, ..., Albin Sandelin, Kristian Helin, Torben Heick Jensen

## Correspondence

helink@mskcc.org (K.H.), thj@mbg.au.dk (T.H.J.)

## In Brief

ZFC3H1 targets pA$^+$ RNA for decay by the nuclear RNA exosome. Garland et al. report a disruptive relationship between excess RNA and PRC2 upon depletion of ZFC3H1 in mouse ESCs. In such conditions, RNA is bound by PRC2 components, which show reduced binding to chromatin and fellow PRC2 proteins.

Garland et al., 2019, Cell Reports *29*, 1800–1811
November 12, 2019 
https://doi.org/10.1016/j.celrep.2019.10.011

CellPress

OPEN ACCESS
CellPress

Cell Reports
Report

# A Functional Link between Nuclear RNA Decay and Transcriptional Control Mediated by the Polycomb Repressive Complex 2

William Garland,[1,2] Itys Comet,[2,3,6] Mengjun Wu,[2,4,6] Aliaksandra Radzisheuskaya,[2,3,5,6] Leonor Rib,[2,4,6] Kristoffer Vitting-Seerup,[2,4] Marta Lloret-Llinares,[1] Albin Sandelin,[2,4] Kristian Helin,[2,3,5,*] and Torben Heick Jensen[1,7,*]

[1]Department of Molecular Biology and Genetics, Aarhus University, Aarhus, Denmark
[2]Biotech Research and Innovation Centre (BRIC), Faculty of Health and Medical Sciences, University of Copenhagen, Copenhagen, Denmark
[3]The Novo Nordisk Foundation for Stem Cell Biology, Faculty of Health and Medical Science, University of Copenhagen, Copenhagen, Denmark
[4]The Bioinformatics Centre, Department of Biology, University of Copenhagen, Copenhagen, Denmark
[5]Cell Biology Program and Center for Epigenetics, Memorial Sloan Kettering Cancer Center, New York, NY, USA
[6]These authors contributed equally
[7]Lead Contact
*Correspondence: helink@mskcc.org (K.H.), thj@mbg.au.dk (T.H.J.)
https://doi.org/10.1016/j.celrep.2019.10.011

## SUMMARY

**Pluripotent embryonic stem cells (ESCs) constitute an essential cellular niche sustained by epigenomic and transcriptional regulation. Any role of post-transcriptional processes remains less explored. Here, we identify a link between nuclear RNA levels, regulated by the poly(A) RNA exosome targeting (PAXT) connection, and transcriptional control by the polycomb repressive complex 2 (PRC2). Knockout of the PAXT component ZFC3H1 impairs mouse ESC differentiation. In addition to the upregulation of bona fide PAXT substrates, *Zfc3h1*$^{-/-}$ cells abnormally express developmental genes usually repressed by PRC2. Such de-repression is paralleled by decreased PRC2 binding to chromatin and low PRC2-directed H3K27 methylation. PRC2 complex stability is compromised in *Zfc3h1*$^{-/-}$ cells with elevated levels of unspecific RNA bound to PRC2 components. We propose that excess RNA hampers PRC2 function through its sequestration from DNA. Our results highlight the importance of balancing nuclear RNA levels and demonstrate the capacity of bulk RNA to regulate chromatin-associated proteins.**

## INTRODUCTION

Embryonic stem cells (ESCs) are distinguished by their dual ability to self-renew and differentiate, both of which require tight regulatory control. ESC pluripotency is maintained by a complex molecular network centered around key transcription factors (TFs), including OCT4, SOX2, NANOG, and KLF2 (Morey et al., 2015; Takahashi and Yamanaka, 2006; Zhou et al., 2007). In addition, epigenetic mechanisms establish and maintain specialized chromatin through DNA methylation and histone modifications to allow the activation and repression of genes during development (Bibikova et al., 2008; Chen and Dent, 2014). In consequence, perturbation of DNA methyltransferases (DNMTs) or chromatin repressive complexes, for example, can disrupt mammalian development through the dysregulation of normal gene expression programs (Laugesen and Helin, 2014; Smith and Meissner, 2013).

The exit of ESCs from pluripotency requires concerted silencing of pluripotency factors and activation of lineage-specific genes (Loebel et al., 2003). A key player here is the polycomb repressive complex 2 (PRC2), which catalyzes the formation of facultative heterochromatin via trimethylation of lysine 27 on histone 3 (H3K27me3). PRC2 is dispensable for the maintenance of self-renewal in ESCs but functions to prevent inappropriate transcriptional activation of lineage-specific differentiation factors. These include highly conserved homeobox (*HOX*) factors, which are crucial for regulating axial patterning in development (Laugesen and Helin, 2014; Pearson et al., 2005), among other developmentally associated TFs that specify cell fate. In ESCs, these genes are repressed through a combination of transcriptional and epigenetic control requiring PRC2 and H3K27me3 (Mallo and Alonso, 2013). Furthermore, PRC2 is crucial for cell fate transitions during development from ESCs, where knockouts (KOs) of core complex components EZH2, SUZ12, and EED result in a block in differentiation (Chamberlain et al., 2008; Pasini et al., 2007; Shen et al., 2008).

Although research on ESC regulation has focused predominantly on transcriptional or epigenetic control, a role of post-transcriptional events, including their putative coupling to transcriptional control, has been less explored. A proper balance of RNA processing and decay ensures homeostasis, whereby different steps in gene regulation buffer one another to maintain a stable expression profile within cell types (for recent reviews see Schmid and Jensen, 2018; Timmers and Tora, 2018). Consequently, malfunction of nuclear RNA decay pathways are therefore linked to developmental disorders and human disease (Corbett, 2018). With improved sequencing technologies, the complexity of the non-protein-coding genome has been revealed (Carninci et al., 2005; Djebali et al., 2012). Functional roles

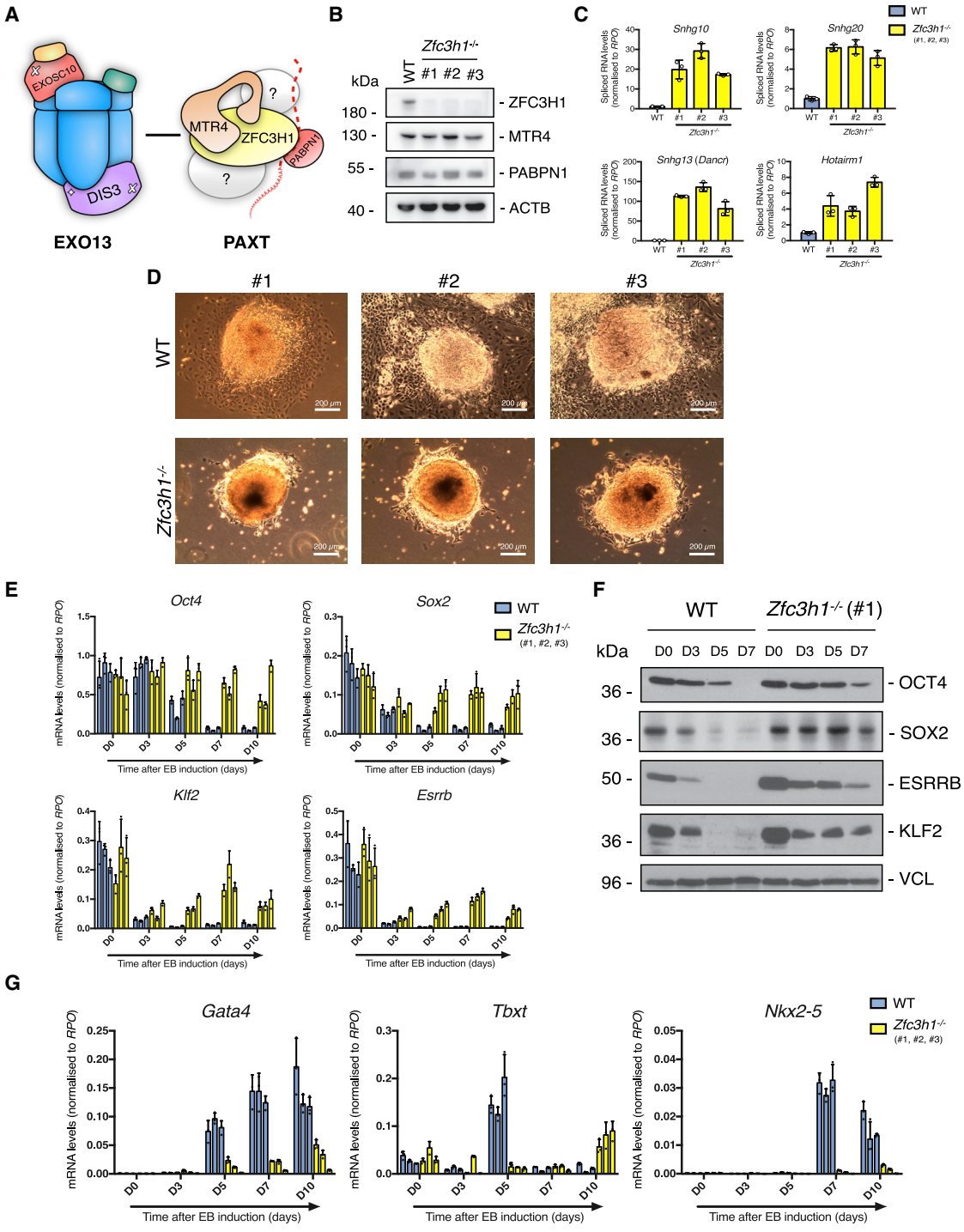


**Figure 1. *Zfc3h1*$^{-/-}$ Cells Display Defects in EB Differentiation**

(A) Schematic representation of the nuclear exosome complex (EXO13) and its PAXT connection. Question marks denote yet-to-be-defined PAXT components.

(B) Western blotting analysis of WT and three independent *Zfc3h1*$^{-/-}$ cell lines (#1–#3). Blots were probed with the indicated PAXT-related antibodies and actin (ACTB) as a loading control.

(C) qRT-PCR analysis of the indicated PAXT targets from total RNA isolated from WT and *Zfc3h1*$^{-/-}$ cell lines. Primers were designed to span exon-exon junctions in order to amplify spliced host gene transcripts. Results are shown relative to Rplp0 mRNA (RPO) and normalized to average WT values. Columns represent average values of technical triplicates per sample, with error bars denoting SD. Individual data values from replicates are indicated as points.

(D) Phase contrast microscopy images of WT and *Zfc3h1*$^{-/-}$ (#1–#3) colonies after 8 days of EB induction. Scale bars denote 200 µm.

*(legend continued on next page)*

have emerged for long non-coding RNAs (lncRNAs), which form ribonucleoprotein (RNP) complexes capable of regulating various stages of gene expression (Geisler and Coller, 2013; Rinn and Chang, 2012), including the maintenance of ESC pluripotency and differentiation (Guttman et al., 2011; Luo et al., 2016). Levels of lncRNAs in eukaryotic nuclei are tightly regulated by RNA decay systems, which consequently must affect biological processes regulated by such transcripts. Furthermore, it has been shown that many key regulators of gene expression also have RNA binding activity (Hendrickson et al., 2016; Khalil et al., 2009). PRC2, for example, binds promiscuously to RNA both *in vitro* and *in vivo*, with all core components (EZH2, SUZ12, and EED) contributing to varying degrees (Cifuentes-Rojas et al., 2014; Davidovich et al., 2013; Zhao et al., 2008, 2010). The function of PRC2-RNA binding is not fully understood, but results have suggested roles of both transcript-mediated recruitment and eviction of PRC2 to and from chromatin (Davidovich et al., 2013; Kaneko et al., 2013; Rinn et al., 2007; da Rocha et al., 2014).

The RNA exosome is an essential 3′-5′ ribonucleolytic complex involved in the regulation of the majority of nuclear transcripts (Kilchert et al., 2016; Mitchell et al., 1997; Schmid and Jensen, 2008). Assessing possible links between transcription regulation and the post-transcriptional balancing of RNA levels, the nuclear exosome stands out with its global activity in the processing of precursor RNAs and its ability to efficiently remove transcriptional by-products and otherwise nuclear retained RNA (Schmid and Jensen, 2018). To facilitate recognition and targeting of its plethora of transcript targets, the nuclear exosome associates with adaptor complexes; that is, two nucleoplasmic decay pathways are guided by the nuclear exosome targeting (NEXT) complex and the poly(A) exosome targeting (PAXT) connection, respectively (Lubas et al., 2011, 2015; Meola et al., 2016; Silla et al., 2018). NEXT and PAXT share a common subunit in the RNA helicase MTR4, which connects these adaptors to the exosome. PAXT is also composed of a large zinc finger protein, ZFC3H1, which bridges MTR4 to the nuclear poly(A) binding protein (PABPN1), aiding the targeting of polyadenylated ($pA^+$) nuclear RNAs for exosome-mediated decay (Beaulieu et al., 2012; Bresson and Conrad, 2013; Meola et al., 2016; Ogami et al., 2017).

At steady state, lncRNA levels in mammalian cells are generally low, with estimates suggesting that less than 1,000 lncRNAs are present in more than one copy per cell (Djebali et al., 2012; Seiler et al., 2017). Thus, most lncRNAs are stoichiometrically inferior to their putative protein effectors, often weakening the associated mechanistic models claiming function of individual lncRNAs. The abundance of lncRNAs is regulated through nuclear RNA decay pathways and is considerably enriched upon removal of exosome components (Lubas et al., 2011; Meola et al., 2016; Silla et al., 2018). Manipulating PAXT activity, through the depletion of ZFC3H1, therefore allows an approach to study the general effects of excess $pA^+$ RNA in the nucleus.

Here, we establish a functional link between PAXT activity and transcriptional control mediated by PRC2. *Zfc3h1*$^{-/-}$ cells are unable to differentiate and exhibit phenotypes reminiscent of cells deficient for PRC2 activity. Consistently, normal PRC2 function is impaired in *Zfc3h1*$^{-/-}$ cells and we provide evidence that this is due to PRC2 binding to stabilized RNAs. Our results highlight the importance of controlling nuclear RNA levels during key regulatory stages of ESC development and imply that modulation of bulk RNA levels is a potent way of lncRNA-mediated transcription regulation.

## RESULTS

### *Zfc3h1*$^{-/-}$ Cells Exhibit Defective Embryoid Body Differentiation

To assess the role of exosome-mediated decay of nuclear $pA^+$ RNAs in ESC pluripotency and differentiation, we used CRISPR/Cas9 to generate homozygous KOs of the PAXT component ZFC3H1 (Figure 1A). *Zfc3h1* was specifically targeted because MTR4 and PABPN1 also reside in alternative nuclear complexes. Three biologically independent *Zfc3h1*$^{-/-}$ ESC lines with disrupted *Zfc3h1* ORFs were derived from single-cell KO clones (Figure S1A). In agreement with our previous observations in human cells, the expression of other known PAXT-related (Figure 1B) and exosome-related (Figure S1B) proteins was unaffected by ZFC3H1 depletion (Meola et al., 2016). Still, PAXT-mediated RNA decay was disrupted, which resulted in an approximately 2-fold accumulation of total nuclear $pA^+$ RNA (Figure S1C), including spliced small nucleolar RNA (snoRNA) host gene (Snhg) lncRNAs (Meola et al., 2016; Figure 1C).

*Zfc3h1*$^{-/-}$ cells were viable under 2i+LIF growth conditions, which selects against cellular differentiation, and appeared morphologically similar to wild-type (WT) cells (Figure S1D). Furthermore, expression of the key pluripotency TFs NANOG, ESRRB, KLF2, SOX2, and OCT4 was not perturbed (Figure S1E), which suggests that the absence of ZFC3H1 does not affect the self-renewal properties of ESCs. Strikingly, however, when cells were transferred from 2i+LIF conditions to serum-LIF media on low-attachment plates to allow the spontaneous development of embryoid bodies (EBs) (Figure S1F), *Zfc3h1*$^{-/-}$ cells displayed morphological phenotypes, suggesting difficulties with normal differentiation. Specifically, after 8 days of EB induction, *Zfc3h1*$^{-/-}$ KO cells still retained an ESC-like morphology, with smaller rounded colonies and a lack of differentiated cell types (Figure 1D). The cells also showed a lack of cystic EBs, cavities that normally form during differentiation because of programmed cell death, but instead remained as solid aggregates, apparent as dark spots on microscopy images (Figure 1D). Finally, between 7 and 8 days of differentiation, WT cells normally develop

(E) qRT-PCR analysis of the indicated mRNAs from total RNA isolated from three independent WT or *Zfc3h1*$^{-/-}$ cell lines taken at the indicated times after induction of EB differentiation (day 0 [D0] to day 10 [D10]). Results are displayed as in (C).
(F) Western blotting analysis of extracts prepared from WT and *Zfc3h1*$^{-/-}$ (#1) cells taken at the indicated times after EB induction (D0–D7). Blots were probed with the indicated antibodies with vinculin (VCL) as a loading control.
(G) qRT-PCR analysis and data representation as described in (E) but using primers against lineage markers (*Gata4*, endoderm; *Tbxt*, mesoderm; *Nkx2-5*, ectoderm).

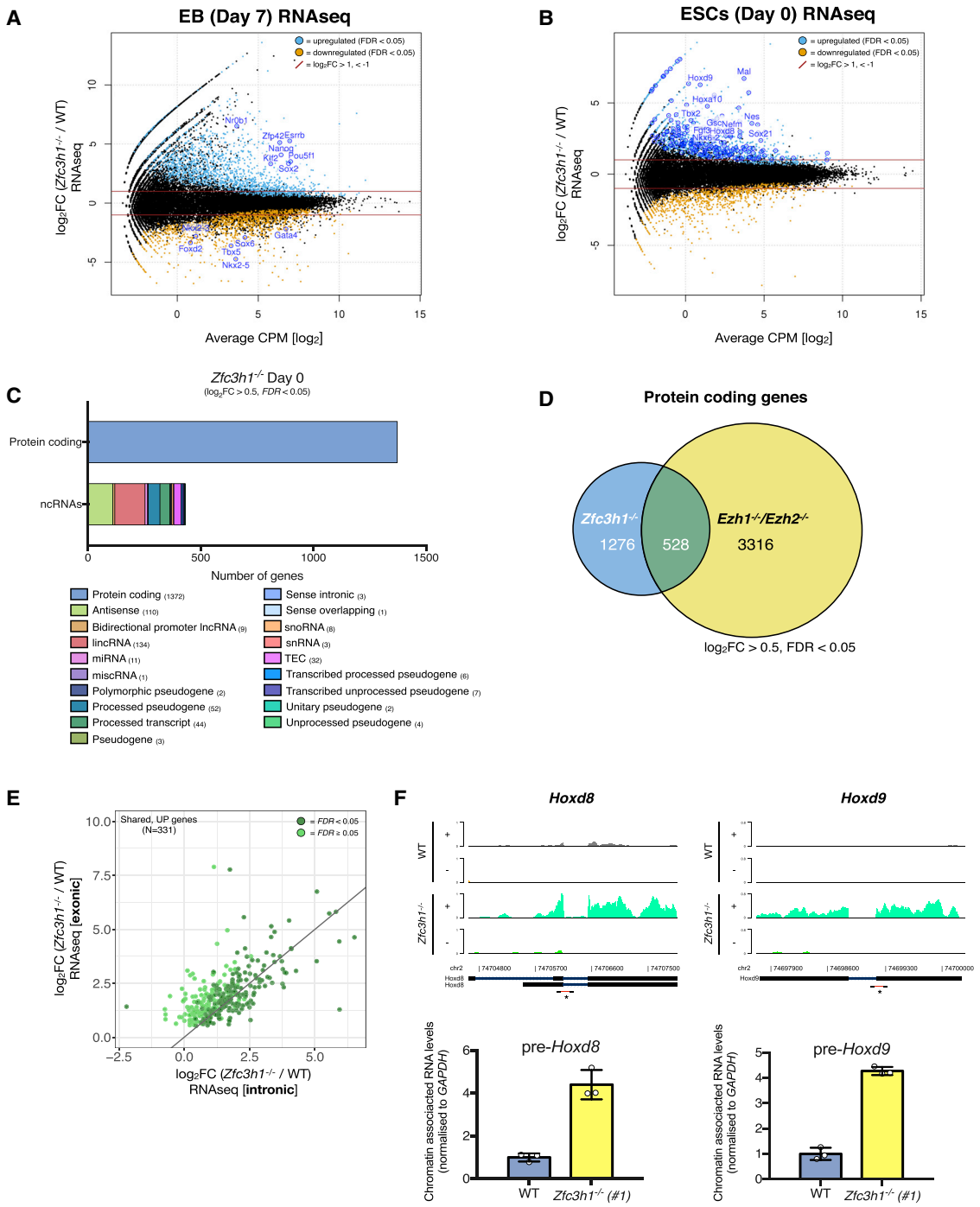


**Figure 2. PRC2 Target Genes Are Upregulated in *Zfc3h1*$^{-/-}$ ESCs**

(A) Differential gene expression analysis of RNA-seq data from *Zfc3h1*$^{-/-}$ versus WT cells after 7 days of EB induction shown as an MA plot. The y axis shows *Zfc3h1*$^{-/-}$ versus WT RNA-seq $\log_2$ FC. The x axis shows average normalized expression as $\log_2$ counts per million (CPM) values across all biological replicates. Each dot indicates a gene, and blue/yellow color denotes significant differential expression (edgeR FDR < 0.05). Red lines denote $\log_2$ FC > 1, <−1. Upregulated genes involved in pluripotency and downregulated genes involved in differentiation are highlighted.

(B) MA plot as in (A) but for undifferentiated (D0) *Zfc3h1*$^{-/-}$ versus WT cells. Values are averages of two WT and three *Zfc3h1*$^{-/-}$ biological replicates. Upregulated genes highlighted indicate PRC2 target genes involved in developmental processes.

(C) Bar plot of upregulated ($\log_2$ FC > 0.5) gene types in D0 *Zfc3h1*$^{-/-}$ cells. GENCODE RNA biotypes are color coded as indicated, and numbers of affected genes are shown in parenthesis.

*(legend continued on next page)*

spontaneous beating colonies, indicative of cardiomyocyte formation (Doetschman et al., 1985), which was not observed up to 10 days of EB induction of *Zfc3h1*$^{-/-}$ cells.

We then collected samples across the EB differentiation time course to analyze the expression of cell type-specific markers (e.g., pluripotency TFs normally decrease rapidly when cells differentiate). In contrast, *Zfc3h1*$^{-/-}$ cells retained high expression of the pluripotency TFs OCT4, SOX2, ESRRB, and KLF2 at later stages of the time course as assessed by RNA and protein analyses (Figures 1E and 1F). qRT-PCR primers spanning exon-intron (ExIn) borders of *Oct4* and *Nr0b1* pre-mRNAs showed that intronic sequences were elevated in *Zfc3h1*$^{-/-}$ cells (Figure S1G), suggesting that these genes might be transcriptionally upregulated. Finally, the expression of lineage-specific markers was impaired in *Zfc3h1*$^{-/-}$ cells, with little or no expression of endodermal, mesodermal, and ectodermal TFs (Figure 1G). Taken together, we conclude that *Zfc3h1*$^{-/-}$ cells show EB differentiation phenotypes and retain an expression profile reminiscent of undifferentiated cells.

## Transcripts from PRC2-Targeted Genes Are Enriched in *Zfc3h1*$^{-/-}$ Cells

To obtain a global impression of the disparities between WT and *Zfc3h1*$^{-/-}$ cells, sequencing of rRNA-depleted total RNA (RNA-seq) was performed on samples harvested after 7 days (D7) of EB induction. This time point was chosen because it showed large gene expression differences between WT and *Zfc3h1*$^{-/-}$ cells as measured by qRT-PCR (Figures 1E and 1G). In addition, total RNA from ESC (D0) samples was sequenced to assess the undifferentiated starting point of the experiment. Biological replicates of RNA-seq libraries were overall highly correlated (Figures S2A and S2B). Differential expression (DE) analysis of D7 samples mirrored our qRT-PCR analyses: *Zfc3h1*$^{-/-}$ cells displayed elevated expression of pluripotency-associated TFs and decreased expression of germ layer-specific transcripts (Figure 2A). This, in conjunction with the morphological phenotypes, suggested that *Zfc3h1*$^{-/-}$ cells are unable to exit from the embryonic stem (ES) state and activate the normal genes required to initiate differentiation. We surmised that this inability to exit from pluripotency might be due to gene expression aberrancies in the D0 ES state disrupting normal progression into differentiation pathways. Consistent with this notion, DE analysis revealed higher levels of mRNAs encoding lineage-specific factors normally associated with differentiated cells in *Zfc3h1*$^{-/-}$ versus WT D0 samples (Figure 2B). A large number of these upregulated lineage markers comprised TFs, including *HOX* genes, which are involved in early developmental processes (Pearson et al., 2005). At first glance, such an expression profile would seemingly contrast our observation that *Zfc3h1*$^{-/-}$ ESCs appear morphologically similar to WT ESCs. However, although exit from pluripotency requires the expression of developmental TFs, this must occur concomitant with suppression of pluripotency TFs, which predominantly define the cellular state of ESCs (Young, 2011). Moreover, the selective pressure of the 2i/LIF culture condition maintains the pluripotent state by blocking *MEK* and *GSK* activity and activating the STAT3 pathway (Wray et al., 2010; Ying et al., 2008).

Nevertheless, abnormal expression of developmental genes in the *Zfc3h1*$^{-/-}$ ESCs indicated a general deregulation of differentiation-associated genes. In WT ESCs, these genes are normally repressed in an inactive chromatin environment highly decorated with H3K27me3 (Mallo and Alonso, 2013). Furthermore, the repression of pluripotency genes during differentiation is regulated by H3K27me3 (Obier et al., 2015; Pasini et al., 2007). As this histone mark is solely catalyzed by the PRC2 complex, we compared the gene expression profile of *Zfc3h1*$^{-/-}$ ESCs with published PRC2 KO (*Ezh1*$^{-/-}$/*Ezh2*$^{-/-}$) RNA-seq data derived from the same parental mouse ESC line (Højfeldt et al., 2018). Of the 1,804 upregulated transcripts in the *Zfc3h1*$^{-/-}$ D0 samples ($\log_2$ fold change [FC] > 0.5, false discovery rate [FDR] < 0.05, edgeR), approximately 25% could be designated as non-coding RNAs (ncRNAs) (Figure 2C), including known PAXT targets upregulated because of their diminished decay, while ~75% of cases were protein coding. Almost one-third of the latter transcripts showed a significant ($p < 1.1e-18$, hypergeometric test) overlap with transcripts upregulated in PRC2 KO cells (Figure 2D). For these shared transcripts, exonic and intronic reads were evenly upregulated in the *Zfc3h1*$^{-/-}$ D0 data (Figure 2E), suggesting that increased mRNA levels were based on increased transcription. This was validated by qRT-PCR analysis of upregulated *HOX* transcripts using ExIn-specific primers on chromatin-associated RNA to enrich for pre-mRNA (Figure 2F). We conclude that *Zfc3h1*$^{-/-}$ ESCs have higher levels of transcripts derived from a subset of PRC2 target loci, and these genes appear to be more transcriptionally active in the absence of PAXT.

## SUZ12 Chromatin Occupancy and H3K27me3 Levels Are Decreased in *Zfc3h1*$^{-/-}$ Cells

As *Zfc3h1*$^{-/-}$ cells displayed increased expression of transcripts also upregulated in the absence of PRC2, we investigated the status of the PRC2 complex in the *Zfc3h1*$^{-/-}$ background. Expression of its core components, EZH2, SUZ12, and EED, was unaffected by the absence of ZFC3H1 (Figure S3A). Therefore, we decided to conduct chromatin immunoprecipitation sequencing (ChIP-seq) on the three *Zfc3h1*$^{-/-}$ cell lines, along

(D) Venn diagram showing overlap of upregulated ($\log_2$ FC > 0.5, FDR < 0.05) protein-coding genes in *Zfc3h1*$^{-/-}$ and *Ezh1*$^{-/-}$/*Ezh2*$^{-/-}$ undifferentiated (D0) cells versus WT cells. The numbers of genes in each set are shown.

(E) Relation between exonic and intronic read counts in *Zfc3h1*$^{-/-}$ and *Ezh1*$^{-/-}$/*Ezh2*$^{-/-}$ upregulated genes. Axes show $\log_2$ FC of normalized RNA-seq reads calculated using edgeR in introns (x) and exons (y) of 331 intron-containing genes upregulated in both *Zfc3h1*$^{-/-}$ and *Ezh1*$^{-/-}$/*Ezh2*$^{-/-}$ RNA-seq datasets (from the intersect in D), with a diagonal reference line (y = x). Dark green dots indicate FDR < 0.05, and light green dots indicate FDR < 0.05 for intronic reads.

(F) Upper panel: Genome Browser views of RNA-seq data from WT and *Zfc3h1*$^{-/-}$ D0 (#1) libraries at the indicated *HOX* gene loci. Tracks show WT and *Zfc3h1*$^{-/-}$ read densities at + and – strands as indicated. RefSeq gene models and mm10 genome coordinates are shown, together with ExIn qRT-PCR primer amplicons used in the lower panel. Lower panel: qRT-PCR analysis of *HOX* gene pre-mRNAs from chromatin-associated RNA isolated from WT and *Zfc3h1*$^{-/-}$ (#1) D0 cells. Results are shown relative to GAPDH mRNA values and normalized to average WT values. Results are displayed as in Figure 1C.

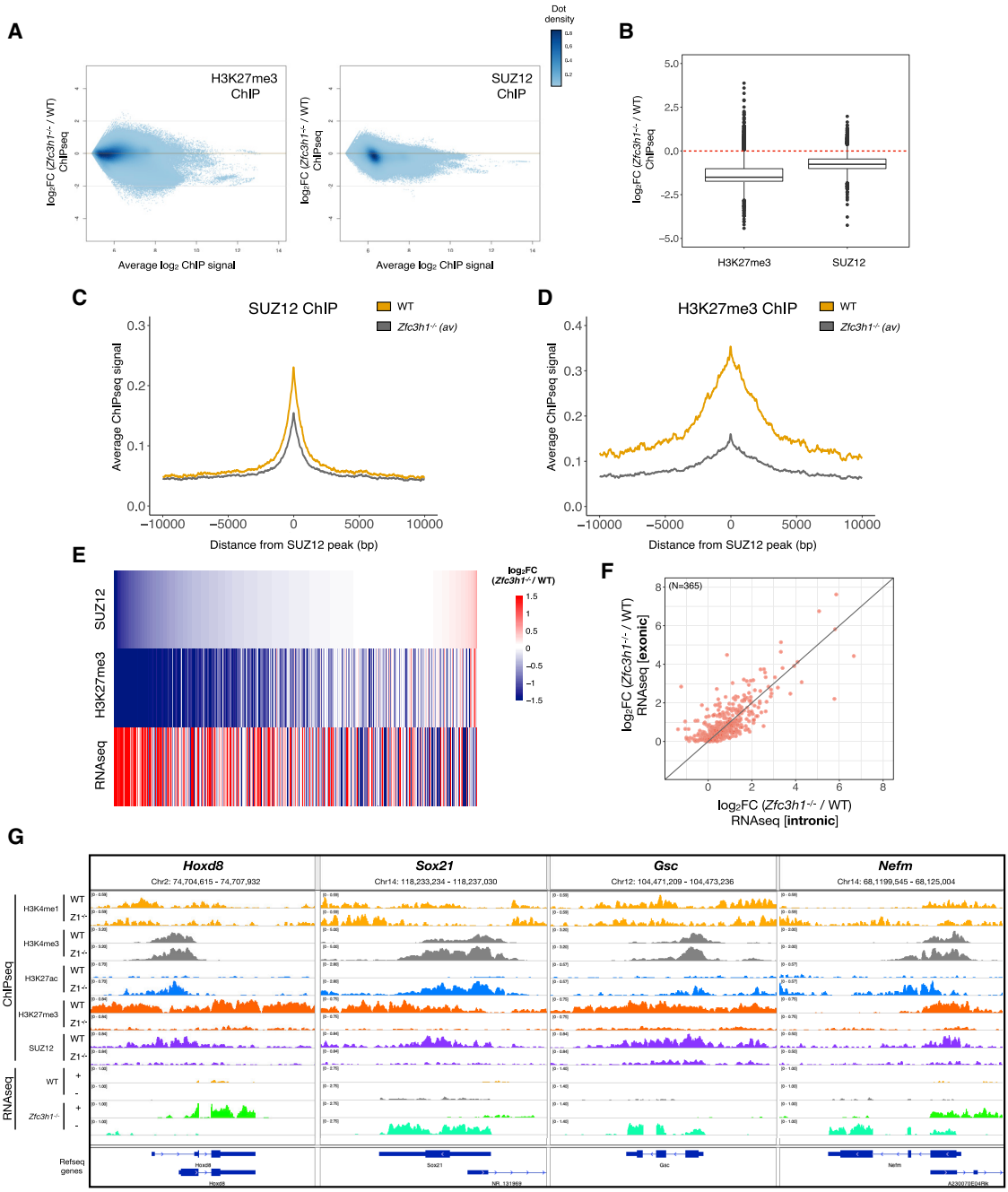


**Figure 3. SUZ12 DNA Occupancy and H3K27me3 Levels Are Decreased in *Zfc3h1*$^{-/-}$ Cells**

(A) MA plots showing global changes in H3K27me3 and SUZ12 ChIP-seq densities in *Zfc3h1*$^{-/-}$ versus WT cell lines. Dots indicate sliding genome windows, where color intensity indicates the density of overlapping points. Y axes show $\log_2$ FC *Zfc3h1*$^{-/-}$ versus WT normalized ChIP signal, and x axes show average $\log_2$ ChIP signal, all from three independent biological replicates.

(B) Boxplot distributions of $\log_2$ FC *Zfc3h1*$^{-/-}$ versus WT normalized H3K27me3 and SUZ12 ChIP signals on regions centered on 3678 SUZ12 peaks identified in WT cells.

(C) Average SUZ12 ChIP-seq signals for *Zfc3h1*$^{-/-}$ and WT cell lines in regions centered on the SUZ12 peaks as in (B). *Zfc3h1*$^{-/-}$ ChIP data are the average of three biological replicates.

(D) As in (C) but for H3K27me3 signal from regions centered on the SUZ12 peaks from (B).

(E) Heatmap representation of the relation between SUZ12 ChIP-seq, H3K27me3 ChIP-seq, and RNA-seq $\log_2$ FC in *Zfc3h1*$^{-/-}$ versus WT cells. Columns represent SUZ12 peaks identified in WT cells (N = 1,485), sorted after SUZ12 *Zfc3h1*$^{-/-}$ versus WT $\log_2$ FC. Rows correspond to SUZ12 ChIP-seq, H3K27me3 ChIP-seq, and RNA-seq *Zfc3h1*$^{-/-}$ versus WT $\log_2$ FC values.

*(legend continued on next page)*

with the parental WT cell line, using antibodies specific for H3K27me3 and SUZ12. *Zfc3h1*$^{-/-}$ cells displayed reduced H3K27me3 levels and SUZ12 DNA occupancy in comparison with WT cells (Figures 3A, S3B, and S3C). These reductions were generally found in regions with high average signal, and the effect on H3K27me3 levels was substantially stronger than the effect on SUZ12 binding (Figure 3B). Still, while H3K27me3 levels were clearly decreased in *Zfc3h1*$^{-/-}$ cells, they were not abolished (average reduction to ~75% versus WT, Figure S3D; as opposed to previously reported KOs of different PRC2 components in which H3K27 methylation is absent, Højfeldt et al., 2018; Pasini et al., 2007; Shen et al., 2008; see Discussion). PRC2-bound regions, defined by SUZ12 ChIP-seq peaks in WT cells, had significantly ($p < 2.2e-16$, one-sided Mann-Whitney test) lower average SUZ12 and H3K27me3 occupancy in *Zfc3h1*$^{-/-}$ conditions (Figures 3B–3D). Moreover, regions depleted for PRC2 and H3K27me3 in *Zfc3h1*$^{-/-}$ cells showed a concomitant increase in RNA expression (Figure 3E), which was equally elevated whether exonic or intronic reads were interrogated (Figure 3F).

ChIP-seq analyses of active and primed chromatin modifications (H3K4me1, H3K4me3, H3K27ac) were also carried out in WT and *Zfc3h1*$^{-/-}$ cells. Genes depleted for SUZ12 and H3K27me3 ChIP signals had a marked increase in H3K27ac levels, concordant with increased RNA transcription (Figures 3G and S3F). We also obtained low-sequence depth RNA polymerase II (RNAPII) ChIP-seq data, which showed increased occupancy at select PRC2 target genes in *Zfc3h1*$^{-/-}$ cells (Figure S3H). Altogether, this fits the notion that PRC2 loci are more transcriptionally active in the absence of normal polycomb-mediated repression via H3K27me3. We conclude that recruitment of SUZ12 to PRC2 target genes is reduced in *Zfc3h1*$^{-/-}$ cells, resulting in loss of H3K27me3 at these regions and abnormal RNA expression due to increased transcription.

## Decreased PRC2 Complex Integrity in *Zfc3h1*$^{-/-}$ Cells

The discovered correlation between PAXT-mediated RNA decay and PRC2-mediated transcriptional repression is unprecedented. We therefore sought to address how impaired PRC2 function in *Zfc3h1*$^{-/-}$ cells relates to the primary phenotype of stabilized nuclear pA$^{+}$ RNAs. As mentioned above, steady-state levels of PRC2 components remain unchanged in *Zfc3h1*$^{-/-}$ cells (Figures S3A, 4A, and 4B, "Inputs"). However, co-immunoprecipitation (coIP) analyses of SUZ12 (Figures 4A and S4A) or EZH2 (Figures 4B and S4B) from whole-cell lysates revealed their reduced binding to the remaining PRC2 core. Similar effects were observed when conducting IPs from nuclear extracts (Figures S4C and S4D). Such weakened PRC2 complex formation in *Zfc3h1*$^{-/-}$ cells was further supported by analyzing the sedimentation of PRC2 components through glycerol gradients: Although the overall protein distribution and sedimentation of loading controls remained unchanged (Figures S4E and S4F), SUZ12 and EZH2 showed a marked shift from high-molecular weight fractions toward lower molecular weight fractions of the gradient derived from *Zfc3h1*$^{-/-}$ lysates (Figures 4C and 4D). The distribution of EED was more dispersed throughout the gradient from WT lysates but still showed a shift toward lower fractions in *Zfch3h1*$^{-/-}$ samples (Figure S1F). Despite these shifts, a fraction of PRC2 sedimented normally in *Zfc3h1*$^{-/-}$ samples and consistently remained bound in coIPs (Figures 4A–4D and S4F). Together, these analyses suggested that the PRC2 complex is partially compromised in *Zfc3h1*$^{-/-}$ cells, which could be further elaborated by subcellular fractionation of WT and *Zfc3h1*$^{-/-}$ cells, giving rise to a slight, but significant, shift in the distribution of SUZ12, EZH2 and EED from chromatin-bound to nucleoplasmic fractions (Figures S4G and S4H). Previous reports demonstrated that the complete loss of SUZ12 or EED results in reduced levels of the remaining PRC2 core components (Højfeldt et al., 2018; Montgomery et al., 2005; Pasini et al., 2007), suggesting that PRC2 complex stability depends on the interactions of all core proteins. In contrast, here we found lower levels of the PRC2 complex in *Zfc3h1*$^{-/-}$ cells despite normal expression of SUZ12, EZH2, and EED.

Given the RNA accumulation observed in the absence of PAXT (Meola et al., 2016; Figures 1C, 2C, and S1C) and the RNA-binding properties of PRC2, we hypothesized that accumulation of PAXT targets could contribute to PRC2 disruption, linking the primary *Zfc3h1*$^{-/-}$ phenotype with a secondary PRC2 phenotype. Hence, we carried out native IPs of SUZ12 and EZH2, using lysates prepared from WT and *Zfc3h1*$^{-/-}$ ESCs, and measured the amount of co-isolated RNA. From WT cells, EZH2 IPs showed a greater enrichment of RNA over SUZ12 IPs and the IgG control (Figure 4E), which is in agreement with EZH2 being the PRC2 component with the strongest capacity for RNA binding (Cifuentes-Rojas et al., 2014). However, elevated RNA levels were isolated from both SUZ12 and EZH2 IPs of *Zfc3h1*$^{-/-}$ versus WT cell lysates. Thus, concomitant with complex disruption, more RNA was bound to PRC2 components upon PAXT depletion. RNA isolated from SUZ12 and EZH2 IPs was sequenced (RIP-seq) to interrogate any differences in PRC2-bound transcripts from WT versus *Zfc3h1*$^{-/-}$ ESCs. Consistent with previous native RIP-seq analysis of PRC2 components (Davidovich et al., 2013; Khalil et al., 2009; Zhao et al., 2010), we found that EZH2 and SUZ12 showed promiscuous binding to both protein-coding RNA and ncRNA. In *Zfc3h1*$^{-/-}$ samples, both SUZ12 and EZH2 RIPs revealed PAXT targets, including pA$^{+}$ nuclear lncRNAs (Figure S5A), along with transcripts from de-repressed PRC2 target genes (Figure S5B). However, for transcripts upregulated in *Zfc3h1*$^{-/-}$ ESCs, there was no significant enrichment of coding RNAs or ncRNAs over the input samples (Figure S5C). Furthermore, there was no specific

(F) Correlation of *Zfc3h1*$^{-/-}$ versus WT $\log_2$ FC RNA-seq signal in intronic versus exonic regions. Points displayed are intron-containing transcripts with $\log_2$ FC > 0 in *Zfc3h1*$^{-/-}$ versus WT overlapping with SUZ12 peaks that show $\log_2$ FC > 0 in *Zfc3h1*$^{-/-}$ ChIP-seq data (N = 365). Axes show *Zfc3h1*$^{-/-}$ versus WT $\log_2$ FC RNA-seq in exonic (y) and intronic (x) regions of these transcripts.

(G) Genome Browser views of four PRC2 target genes (*Hoxd8*, *Sox21*, *Gsc*, and *Nefm*). Displayed tracks include H3K4me1, H3K4me3, H3K27ac, H3K27me3, and SUZ12 ChIP-seq data as well as RNA-seq data from WT and *Zfc3h1*$^{-/-}$ (#1) cell lines. RNA-seq tracks on both strands are shown (+ and –, respectively). Gene models are based on RefSeq. Genome coordinates (mm10) are indicated for each panel.

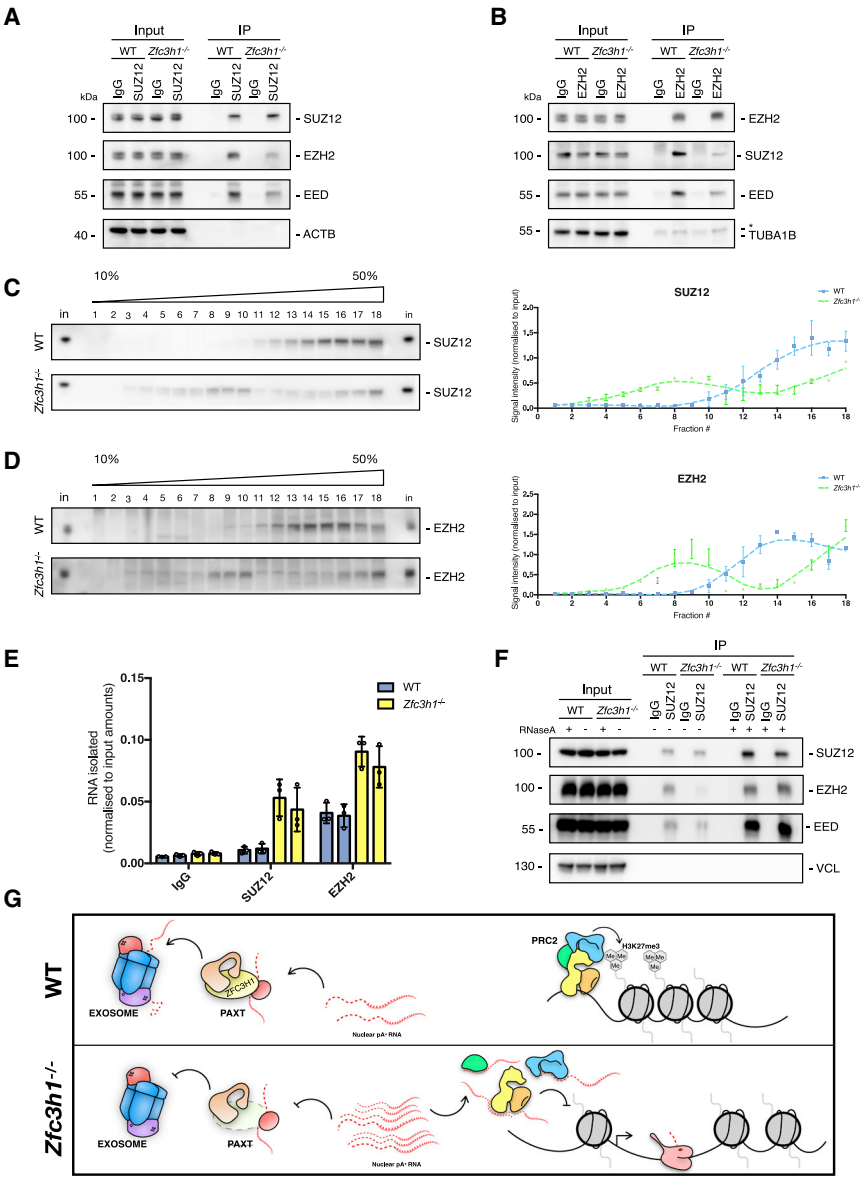


**Figure 4. Decreased PRC2 Complex Integrity in *Zfc3h1*$^{-/-}$ Cells**

(A) Western blotting analysis of SUZ12 IPs from lysates of WT and *Zfc3h1*$^{-/-}$ cells. IgG IPs were included as a negative control. Input and IP samples were probed using the indicated antibodies. Actin (ACTB) was used as an input loading control.

(B) Western blotting analysis as in (A) but for EZH2 IPs. Tubulin (TUBA1B) was used as an input loading control.

(C) Glycerol gradient analysis of SUZ12 sedimentation in extracts from WT and *Zfc3h1*$^{-/-}$ cells. Left panel: western blotting analysis of 10%–50% glycerol gradient fractions. Right panel: quantification of SUZ12 signals from the western blotting analysis. Fraction values were normalized to input sample signals. Points show the average signal from duplicate samples and error bars denote the SD. A smoothed curve was plotted to indicate the distribution of signal throughout the gradient.

(D) As in (C), but showing EZH2 distribution throughout the gradients.

(E) Quantification of RNA isolated from IgG, SUZ12, or EZH2 IPs of WT or *Zfc3h1*$^{-/-}$ cell lysates. Values were normalized to input samples. Columns represent the average value of technical triplicates per sample, with error bars denoting SD. Individual data values from technical triplicates are indicated as points.

(F) Western blotting analysis of SUZ12 IPs from WT or *Zfc3h1*$^{-/-}$ lysates following either mock or RNaseA treatment. Input and IP samples were probed as in (A) but with vinculin (VCL) as an input loading control.

(G) Summary depicting the suggested functional consequences of *Zfc3h1*$^{-/-}$ KOs in ESCs. In the absence of PAXT-mediated RNA decay, nuclear pA$^{+}$ transcripts are stabilized. Excess RNA binds and out-titrates PRC2 from chromatin, and the interaction between complex subunits is disrupted. PRC2-depleted regions show reduced H3K27me3 levels and correlate with increased transcription at affected loci.

enrichment of RNAs upregulated in *Zfc3h1*$^{-/-}$ ESCs only, in both *Zfc3h1*$^{-/-}$ and *Ezh1*$^{-/-}$*Ezh2*$^{-/-}$ ESCs (Højfeldt et al., 2018) or for transcripts upregulated at SUZ12-depleted loci (Figure S5D). This suggests that increased nuclear RNA levels in *Zfc3h1*$^{-/-}$ ESCs leads to more RNA binding to PRC2 components with no general specificity.

To address whether the disruption of PRC2 in *Zfc3h1*$^{-/-}$ cells was indeed dependent on increased RNA levels, we repeated the SUZ12 coIP analyses using cell extracts that were either mock or RNaseA treated. In the presence of RNase, SUZ12 IPs from *Zfc3h1*$^{-/-}$ extracts recapitulated the coIP efficiency of equivalent WT extracts (Figures 4F and S5E). More bait protein was generally pulled down in the RNase-treated samples, which suggested that RNA already interfered with the IP in WT extracts, but to a greater extent in *Zfc3h1*$^{-/-}$ extracts. Taken together, we propose that increased RNA binding weakens PRC2 complex formation, thereby decreasing its normal function, stability. and recruitment to chromatin (Figure 4G; see Discussion).

## DISCUSSION

The molecular decisions that govern correct progression through cellular differentiation require a complex agreement of checks and balances. Here, the transcriptional and epigenetic profiles at the ESC stage are important starting points, whose dysregulation may be deleterious for development. In the present study, we discovered a link between excess nuclear RNA and PRC2-mediated transcriptional control in ESCs, suggesting an essential role of nuclear RNA turnover in cellular commitment to differentiation.

Deletion of the nuclear exosome adaptor ZFC3H1 to some extent phenocopies ESCs depleted for PRC2 components; cells

self-renew and appear morphologically similar to WT cells but show a loss of H3K27me3, deregulation of PRC2 target genes, and difficulty initiating differentiation (Boyer et al., 2006; Chamberlain et al., 2008; Pasini et al., 2007; Shen et al., 2008). In contrast to PRC2-depleted cells, *Zfc3h1*$^{-/-}$ ESCs retain a degree of SUZ12 binding and H3K27me3 modification, which presumably explains the less severe deregulation of PRC2 target genes. Still, the defect appears to be sufficient to restrict the progression into differentiation. In agreement with previous studies, we find that deregulation of PRC2 target genes results in abnormal transcription of developmental genes (Boyer et al., 2006; Lee et al., 2006). It would seem counterintuitive for ESCs expressing developmental genes to retain self-renewal ability and to lose the ability to differentiate upon induction of EB formation. However, it has been suggested that the expression of pluripotency TFs is sufficient for self-renewal and overrides any abnormal expression of lineage markers (Chamberlain et al., 2008). As cells exit pluripotency, PRC2 functions to silence key maintenance factors such as *Oct4*, *Sox2*, and *Nanog* by depositing H3K27me3 at their loci (Obier et al., 2015). With PRC2 function decreased in *Zfc3h1*$^{-/-}$ cells, this presumably explains their retained transcriptional activity of pluripotency TFs and block in differentiation (Figures 1E, 1F, and S1G). Together this reiterates that PRC2 and, in turn, ZFC3H1 are dispensable for self-renewal but are essential for the progression into differentiation (Chamberlain et al., 2008; Pasini et al., 2007; Shen et al., 2008).

An RNA-binding ability of the PRC2 complex has been widely documented, with suggested models for transcript-mediated recruitment or eviction of PRC2 to or from DNA (Davidovich et al., 2013; Kaneko et al., 2013; Rinn et al., 2007; da Rocha et al., 2014). A primary phenotype of ZFC3H1 depletion is the stabilization of nuclear pA$^{+}$ RNAs (Meola et al., 2016; Ogami et al., 2017; this study), which are, by nature, unstable and typically present only in trace amounts under normal conditions. Through removing the targeting mechanisms for decay, this increases the concentration of pA$^{+}$ RNAs (Silla et al., 2018). Taken together with increased binding of RNA to EZH2 and SUZ12 in *Zfc3h1*$^{-/-}$ cells, we therefore propose that increased transcript levels negatively affect PRC2 function through its increased RNA binding (Figure 4G). Previous studies initially suggested that excess RNA can inhibit the methyltransferase activity of EZH2 *in vitro* (Cifuentes-Rojas et al., 2014; Kaneko et al., 2014), which was further elaborated to suggest that decreased catalytic activity was due to RNA titrating PRC2 off nucleosomes (Wang et al., 2017). This was supported by observations that DNA- and RNA-binding capabilities of PRC2 are mutually exclusive *in vitro* (Beltran et al., 2016; Wang et al., 2017). More recently, an RNA-binding region was identified at an allosteric regulatory region of PRC2 in close proximity to the methyltransferase region of EZH2, which is subsequently inhibited by RNA binding (Zhang et al., 2019). It is therefore plausible that increased nuclear RNA levels dually affect PRC2 function by decreasing its catalytic activity as well as its DNA-binding capacity. We also find that the interaction between PRC2 subunits is compromised in *Zfc3h1*$^{-/-}$ cells with reduced binding between core subunits in coIP and glycerol gradient assays (Figures 4A–4D). Such decreased interaction between SUZ12 and EZH2 may contribute to an explanation of the stronger loss of H3K27me3 compared with SUZ12 ChIP-seq signal in *Zfc3h1*$^{-/-}$ cells (Figure 3B); that is, residual SUZ12, uncoupled from EZH2, may still bind DNA. In line with this, our ChIP and subcellular fractionation data showed that a fraction of PRC2 components are still associated with chromatin. This partial phenotype allows us only to speculate at this point and will require further investigation to understand the status of PRC2 complex proteins that are still able to bind DNA. However, in support of this possibility, the N-terminal region of SUZ12 recapitulates SUZ12-binding patterns but lacks EZH2 interaction and thereby does not rescue H3K27me3 activity (Højfeldt et al., 2018). The use of such mutants, in combination with *Zfc3h1*$^{-/-}$ cells and extended ChIP datasets, might allow unpacking of the molecular basis behind these observations.

Finally, we show that the disruption between core PRC2 subunits in *Zfc3h1*$^{-/-}$ cell extracts can be rescued upon RNase treatment (Figure 4F). These results echo previous data showing that RNase treatment increases chromatin association of PRC2 in cells and, reciprocally, recombinant PRC2 can be titrated off nucleosomes by increasing nuclear RNA levels (Beltran et al., 2016). We propose that this antagonism is a general effect of increased nuclear RNA, as we do not see specific enrichment of particular transcripts in RIP-seq experiments: RNAs that are upregulated in the *Zfc3h1*$^{-/-}$ inputs are also upregulated in the RIP data. This appears in line with previous findings, that the RNA-binding capability of PRC2 is non-specific and promiscuous in nature.

Although PRC2 has garnered considerable attention, RNA-binding capacities have also been reported for other chromatin regulators, including DNMTs, histone deacetylases (HDAC1), chromatin remodeling proteins (ATRX), DNA demethylases (TET1/2), and other histone methyltransferases (G9a) (Castellanos-Rubio et al., 2016; He et al., 2016; Hendrickson et al., 2016; Holz-Schietinger and Reich, 2012; Li et al., 2018; Di Ruscio et al., 2013; Sarma et al., 2014). Interestingly, RNA has been suggested to have a regulatory function in a number of models, either locally at specific loci or by more global mechanisms; that is, similar to PRC2, RNA binding has been proposed to sequester DNMT1 from transcriptionally active regions as a regulatory mechanisms to prevent DNA methylation at these loci (Di Ruscio et al., 2013). Indeed, RIP experiments demonstrate that SUZ12 and DNMT1 both tend to associate with the 5′ ends of RNA (Hendrickson et al., 2016), and both proteins have a greater affinity for RNA over DNA (Di Ruscio et al., 2013; Wang et al., 2017). RNA sequestering is also suggested in some disease models in which lncRNAs are overexpressed and affect chromatin modifiers through their abnormal titration (Gupta et al., 2010; Li et al., 2018; Merry et al., 2015; Prensner et al., 2013). Taken together with our results, this highlights the importance of maintaining a stable nuclear transcriptome through active RNA decay to prevent off-target effects as a result of RNA accumulation. Moreover, our results demonstrate the capacity of changed bulk RNA levels to affect cellular transcription programs. Although dysregulation of PRC2 on a global level is highlighted here, it is equally feasible that an unbalanced transcriptome might affect the function of other bivalent chromatin/RNA-binding proteins either locally or globally.

## STAR★METHODS

Detailed methods are provided in the online version of this paper and include the following:

- KEY RESOURCES TABLE
- LEAD CONTACT AND MATERIALS AVAILABILITY
- EXPERIMENTAL MODEL AND SUBJECT DETAILS
  - mES cell culture and differentiation
- METHOD DETAILS
  - CRISPR/Cas9 KOs
  - RNA isolation
  - $pA^+$ RNA purification
  - qRT-PCR analysis
  - RNA-seq library preparation
  - Western blotting analysis
  - IP experiments
  - Glycerol gradient sedimentation analysis
  - RNaseA treatment
  - Subcellular fractionation
  - RIP experiments
  - RIP-seq
  - ChIP experiments
- QUANTIFICATION AND STATISTICAL ANALYSIS
  - Processing and analysis of RNA-seq data
  - Processing and analysis of RIP-seq data
  - Processing and analysis of ChIP-seq data
- DATA AND CODE AVAILABILITY

## SUPPLEMENTAL INFORMATION

Supplemental Information can be found online at https://doi.org/10.1016/j.celrep.2019.10.011.

## ACKNOWLEDGMENTS

We thank Nadia Laurs Schmidt, Dorthe Riishøj, and Anna Fossum for excellent technical assistance; Manfred Schmid and Peter Refsing Andersen for critical comments; and members of the T.H.J., K.H., and A.S. groups for advice and discussion. Work in the T.H.J. laboratory was supported by the European Research Council (ERC) (grant 339953), the Lundbeck Foundation, and Novo Nordisk Foundation (NNF). A.R. was funded by the European Union's Horizon 2020 research and innovation program under Marie Skłodowska-Curie Actions grant agreement 749362. Work in the K.H. laboratory was supported by the NNF (NNF16OC0023234), through a center grant from the NNF to the NNF Center for Stem Cell Biology (NNF17CC0027852) and through the Memorial Sloan Kettering Cancer Center Support Grant (NIH grant P30 CA008748). Work in the A.S. laboratory was funded by the Lundbeck Foundation.

## AUTHOR CONTRIBUTIONS

W.G., A.S., K.H., and T.H.J. conceived the project. W.G. designed and performed the majority of experiments. I.C. performed the ChIP experiments. M.W., L.R., and K.V.S. carried out the bioinformatics analysis. A.R. and M.L.-L. contributed to the experimental design and cell line generation. T.H.J., K.H., and A.S. supervised the project. W.G. and T.H.J. wrote the manuscript with input from all co-authors.

## DECLARATION OF INTERESTS

The authors declare no competing interests.

Received: May 8, 2019
Revised: August 28, 2019
Accepted: October 2, 2019
Published: November 12, 2019

## REFERENCES

Ambrosini, G., Dreos, R., Kumar, S., and Bucher, P. (2016). The ChIP-seq tools and web server: a resource for analyzing ChIP-seq and other types of genomic data. BMC Genomics *17*, 938.

Beaulieu, Y.B., Kleinman, C.L., Landry-Voyer, A.M., Majewski, J., and Bachand, F. (2012). Polyadenylation-dependent control of long noncoding RNA expression by the poly(A)-binding protein nuclear 1. PLoS Genet. *8*, e1003078.

Beltran, M., Yates, C.M., Skalska, L., Dawson, M., Reis, F.P., Viiri, K., Fisher, C.L., Sibley, C.R., Foster, B.M., Bartke, T., et al. (2016). The interaction of PRC2 with RNA or chromatin is mutually antagonistic. Genome Res. *26*, 896–907.

Bibikova, M., Laurent, L.C., Ren, B., Loring, J.F., and Fan, J.B. (2008). Unraveling epigenetic regulation in embryonic stem cells. Cell Stem Cell *2*, 123–134.

Bolger, A.M., Lohse, M., and Usadel, B. (2014). Trimmomatic: a flexible trimmer for Illumina sequence data. Bioinformatics *30*, 2114–2120.

Boyer, L.A., Plath, K., Zeitlinger, J., Brambrink, T., Medeiros, L.A., Lee, T.I., Levine, S.S., Wernig, M., Tajonar, A., Ray, M.K., et al. (2006). Polycomb complexes repress developmental regulators in murine embryonic stem cells. Nature *441*, 349–353.

Bracken, A.P., Pasini, D., Capra, M., Prosperini, E., Colli, E., and Helin, K. (2003). EZH2 is downstream of the pRB-E2F pathway, essential for proliferation and amplified in cancer. EMBO J. *22*, 5323–5335.

Bresson, S.M., and Conrad, N.K. (2013). The human nuclear poly(a)-binding protein promotes RNA hyperadenylation and decay. PLoS Genet. *9*, e1003893.

Brouwer, R., Allmang, C., Raijmakers, R., van Aarssen, Y., Egberts, W.V., Petfalski, E., van Venrooij, W.J., Tollervey, D., and Pruijn, G.J.M. (2001). Three novel components of the human exosome. J. Biol. Chem. *276*, 6177–6184.

Candiano, G., Bruschi, M., Musante, L., Santucci, L., Ghiggeri, G.M., Carnemolla, B., Orecchia, P., Zardi, L., and Righetti, P.G. (2004). Blue silver: a very sensitive colloidal Coomassie G-250 staining for proteome analysis. Electrophoresis *25*, 1327–1333.

Carninci, P., Kasukawa, T., Katayama, S., Gough, J., Frith, M.C., Maeda, N., Oyama, R., Ravasi, T., Lenhard, B., Wells, C., et al. (2005). The transcriptional landscape of the mammalian genome. Science *309*, 1559–1563.

Castellanos-Rubio, A., Fernandez-Jimenez, N., Kratchmarov, R., Luo, X., Bhagat, G., Green, P.H.R., Schneider, R., Kiledjian, M., Bilbao, J.R., and Ghosh, S. (2016). A long noncoding RNA associated with susceptibility to celiac disease. Science *352*, 91–96.

Chamberlain, S.J., Yee, D., and Magnuson, T. (2008). Polycomb repressive complex 2 is dispensable for maintenance of embryonic stem cell pluripotency. Stem Cells *26*, 1496–1505.

Chen, T., and Dent, S.Y.R. (2014). Chromatin modifiers and remodellers: regulators of cellular differentiation. Nat. Rev. Genet. *15*, 93–106.

Chu, C.S., Lo, P.W., Yeh, Y.H., Hsu, P.H., Peng, S.H., Teng, Y.C., Kang, M.L., Wong, C.H., and Juan, L.J. (2014). O-GlcNAcylation regulates EZH2 protein stability and function. Proc. Natl. Acad. Sci. U S A *111*, 1355–1360.

Cifuentes-Rojas, C., Hernandez, A.J., Sarma, K., and Lee, J.T. (2014). Regulatory interactions between RNA and polycomb repressive complex 2. Mol. Cell *55*, 171–185.

Conrad, T., and Ørom, U.A. (2017). Cellular Fractionation and Isolation of Chromatin-Associated RNA (Humana Press), pp. 1–9.

Corbett, A.H. (2018). Post-transcriptional regulation of gene expression and human disease. Curr. Opin. Cell Biol. *52*, 96–104.

da Rocha, S.T., Boeva, V., Escamilla-Del-Arenal, M., Ancelin, K., Granier, C., Matias, N.R., Sanulli, S., Chow, J., Schulz, E., Picard, C., et al. (2014). Jarid2

is implicated in the initial Xist-induced targeting of PRC2 to the inactive X chromosome. Mol. Cell *53*, 301–316.

Davidovich, C., Zheng, L., Goodrich, K.J., and Cech, T.R. (2013). Promiscuous RNA binding by Polycomb repressive complex 2. Nat. Struct. Mol. Biol. *20*, 1250–1257.

Di Ruscio, A., Ebralidze, A.K., Benoukraf, T., Amabile, G., Goff, L.A., Terragni, J., Figueroa, M.E., De Figueiredo Pontes, L.L., Alberich-Jorda, M., Zhang, P., et al. (2013). DNMT1-interacting RNAs block gene-specific DNA methylation. Nature *503*, 371–376.

Djebali, S., Davis, C.A., Merkel, A., Dobin, A., Lassmann, T., Mortazavi, A., Tanzer, A., Lagarde, J., Lin, W., Schlesinger, F., et al. (2012). Landscape of transcription in human cells. Nature *489*, 101–108.

Doetschman, T.C., Eistetter, H., Katz, M., Schmidt, W., and Kemler, R. (1985). The in vitro development of blastocyst-derived embryonic stem cell lines: formation of visceral yolk sac, blood islands and myocardium. J. Embryol. Exp. Morphol. *87*, 27–45.

ENCODE Project Consortium (2012). An integrated encyclopedia of DNA elements in the human genome. Nature *489*, 57–74.

Frankish, A., Diekhans, M., Ferreira, A.M., Johnson, R., Jungreis, I., Loveland, J., Mudge, J.M., Sisu, C., Wright, J., Armstrong, J., et al. (2019). GENCODE reference annotation for the human and mouse genomes. Nucleic Acids Res. *47* (*D1*), D766–D773.

Geisler, S., and Coller, J. (2013). RNA in unexpected places: long non-coding RNA functions in diverse cellular contexts. Nat. Rev. Mol. Cell Biol. *14*, 699–712.

Gupta, R.A., Shah, N., Wang, K.C., Kim, J., Horlings, H.M., Wong, D.J., Tsai, M.C., Hung, T., Argani, P., Rinn, J.L., et al. (2010). Long non-coding RNA HOTAIR reprograms chromatin state to promote cancer metastasis. Nature *464*, 1071–1076.

Guttman, M., Donaghey, J., Carey, B.W., Garber, M., Grenier, J.K., Munson, G., Young, G., Lucas, A.B., Ach, R., Bruhn, L., et al. (2011). lincRNAs act in the circuitry controlling pluripotency and differentiation. Nature *477*, 295–300.

He, C., Sidoli, S., Warneford-Thomson, R., Tatomer, D.C., Wilusz, J.E., Garcia, B.A., and Bonasio, R. (2016). High-resolution mapping of RNA-binding regions in the nuclear proteome of embryonic stem cells. Mol. Cell *64*, 416–430.

Hendrickson, D.G., Kelley, D.R., Tenen, D., Bernstein, B., and Rinn, J.L. (2016). Widespread RNA binding by chromatin-associated proteins. Genome Biol. *17*, 28.

Højfeldt, J.W., Laugesen, A., Willumsen, B.M., Damhofer, H., Hedehus, L., Tvardovskiy, A., Mohammad, F., Jensen, O.N., and Helin, K. (2018). Accurate H3K27 methylation can be established de novo by SUZ12-directed PRC2. Nat. Struct. Mol. Biol. *25*, 225–232.

Holz-Schietinger, C., and Reich, N.O. (2012). RNA modulation of the human DNA methyltransferase 3A. Nucleic Acids Res. *40*, 8550–8557.

Kaneko, S., Son, J., Shen, S.S., Reinberg, D., and Bonasio, R. (2013). PRC2 binds active promoters and contacts nascent RNAs in embryonic stem cells. Nat. Struct. Mol. Biol. *20*, 1258–1264.

Kaneko, S., Son, J., Bonasio, R., Shen, S.S., and Reinberg, D. (2014). Nascent RNA interaction keeps PRC2 activity poised and in check. Genes Dev. *28*, 1983–1988.

Kent, W.J., Zweig, A.S., Barber, G., Hinrichs, A.S., and Karolchik, D. (2010). BigWig and BigBed: enabling browsing of large distributed datasets. Bioinformatics *26*, 2204–2207.

Khalil, A.M., Guttman, M., Huarte, M., Garber, M., Raj, A., Rivea Morales, D., Thomas, K., Presser, A., Bernstein, B.E., van Oudenaarden, A., et al. (2009). Many human large intergenic noncoding RNAs associate with chromatin-modifying complexes and affect gene expression. Proc. Natl. Acad. Sci. U S A *106*, 11667–11672.

Kilchert, C., Wittmann, S., and Vasiljeva, L. (2016). The regulation and functions of the nuclear RNA exosome complex. Nat. Rev. Mol. Cell Biol. *17*, 227–239.

Kim, D., Langmead, B., and Salzberg, S.L. (2015). HISAT: a fast spliced aligner with low memory requirements. Nat. Methods *12*, 357–360.

Langmead, B., and Salzberg, S.L. (2012). Fast gapped-read alignment with Bowtie 2. Nat. Methods *9*, 357–359.

Laugesen, A., and Helin, K. (2014). Chromatin repressive complexes in stem cells, development, and cancer. Cell Stem Cell *14*, 735–751.

Lee, T.I., Jenner, R.G., Boyer, L.A., Guenther, M.G., Levine, S.S., Kumar, R.M., Chevalier, B., Johnstone, S.E., Cole, M.F., Isono, K., et al. (2006). Control of developmental regulators by Polycomb in human embryonic stem cells. Cell *125*, 301–313.

Lerdrup, M., Johansen, J.V., Agrawal-Singh, S., and Hansen, K. (2016). An interactive environment for agile analysis and visualization of ChIP-sequencing data. Nat. Struct. Mol. Biol. *23*, 349–357.

Li, H., Handsaker, B., Wysoker, A., Fennell, T., Ruan, J., Homer, N., Marth, G., Abecasis, G., and Durbin, R.; 1000 Genome Project Data Processing Subgroup (2009). The Sequence Alignment/Map format and SAMtools. Bioinformatics *25*, 2078–2079.

Li, Q., Dong, C., Cui, J., Wang, Y., and Hong, X. (2018). Over-expressed lncRNA HOTAIRM1 promotes tumor growth and invasion through up-regulating HOXA1 and sequestering G9a/EZH2/Dnmts away from the HOXA1 gene in glioblastoma multiforme. J. Exp. Clin. Cancer Res. *37*, 265.

Liao, Y., Smyth, G.K., and Shi, W. (2013). The Subread aligner: fast, accurate and scalable read mapping by seed-and-vote. Nucleic Acids Res. *41*, e108–e108.

Loebel, D.A.F., Watson, C.M., De Young, R.A., and Tam, P.P.L. (2003). Lineage choice and differentiation in mouse embryos and embryonic stem cells. Dev. Biol. *264*, 1–14.

Lubas, M., Christensen, M.S., Kristiansen, M.S., Domanski, M., Falkenby, L.G., Lykke-Andersen, S., Andersen, J.S., Dziembowski, A., and Jensen, T.H. (2011). Interaction profiling identifies the human nuclear exosome targeting complex. Mol. Cell *43*, 624–637.

Lubas, M., Andersen, P.R., Schein, A., Dziembowski, A., Kudla, G., and Jensen, T.H. (2015). The human nuclear exosome targeting complex is loaded onto newly synthesized RNA to direct early ribonucleolysis. Cell Rep. *10*, 178–192.

Luo, S., Lu, J.Y., Liu, L., Yin, Y., Chen, C., Han, X., Wu, B., Xu, R., Liu, W., Yan, P., et al. (2016). Divergent lncRNAs regulate gene expression and lineage differentiation in pluripotent cells. Cell Stem Cell *18*, 637–652.

Mallo, M., and Alonso, C.R. (2013). The regulation of Hox gene expression during animal development. Development *140*, 3951–3963.

McCarthy, D.J., Chen, Y., and Smyth, G.K. (2012). Differential expression analysis of multifactor RNA-Seq experiments with respect to biological variation. Nucleic Acids Res. *40*, 4288–4297.

McKenna, A., Hanna, M., Banks, E., Sivachenko, A., Cibulskis, K., Kernytsky, A., Garimella, K., Altshuler, D., Gabriel, S., Daly, M., and DePristo, M.A. (2010). The Genome Analysis Toolkit: a MapReduce framework for analyzing next-generation DNA sequencing data. Genome Res. *20*, 1297–1303.

Meola, N., Domanski, M., Karadoulama, E., Chen, Y., Gentil, C., Pultz, D., Vitting-Seerup, K., Lykke-Andersen, S., Andersen, J.S., Sandelin, A., and Jensen, T.H. (2016). Identification of a nuclear exosome decay pathway for processed transcripts. Mol. Cell *64*, 520–533.

Merry, C.R., Forrest, M.E., Sabers, J.N., Beard, L., Gao, X.H., Hatzoglou, M., Jackson, M.W., Wang, Z., Markowitz, S.D., and Khalil, A.M. (2015). DNMT1-associated long non-coding RNAs regulate global gene expression and DNA methylation in colon cancer. Hum. Mol. Genet. *24*, 6240–6253.

Mitchell, P., Petfalski, E., Shevchenko, A., Mann, M., and Tollervey, D. (1997). The exosome: a conserved eukaryotic RNA processing complex containing multiple 3′–>5′ exoribonucleases. Cell *91*, 457–466.

Montgomery, N.D., Yee, D., Chen, A., Kalantry, S., Chamberlain, S.J., Otte, A.P., and Magnuson, T. (2005). The murine polycomb group protein Eed is required for global histone H3 lysine-27 methylation. Curr. Biol. *15*, 942–947.

Morey, L., Santanach, A., and Di Croce, L. (2015). Pluripotency and epigenetic factors in mouse embryonic stem cell fate regulation. Mol. Cell. Biol. *35*, 2716–2728.

Obier, N., Lin, Q., Cauchy, P., Hornich, V., Zenke, M., Becker, M., and Müller, A.M. (2015). Polycomb protein EED is required for silencing of pluripotency genes upon ESC differentiation. Stem Cell Rev Rep *11*, 50–61.

Ogami, K., Richard, P., Chen, Y., Hoque, M., Li, W., Moresco, J.J., Yates, J.R., 3rd, Tian, B., and Manley, J.L. (2017). An Mtr4/ZFC3H1 complex facilitates turnover of unstable nuclear RNAs to prevent their cytoplasmic transport and global translational repression. Genes Dev. *31*, 1257–1271.

Pasini, D., Bracken, A.P., Hansen, J.B., Capillo, M., and Helin, K. (2007). The polycomb group protein Suz12 is required for embryonic stem cell differentiation. Mol. Cell. Biol. *27*, 3769–3779.

Pearson, J.C., Lemons, D., and McGinnis, W. (2005). Modulating Hox gene functions during animal body patterning. Nat. Rev. Genet. *6*, 893–904.

Prensner, J.R., Iyer, M.K., Sahu, A., Asangani, I.A., Cao, Q., Patel, L., Vergara, I.A., Davicioni, E., Erho, N., Ghadessi, M., et al. (2013). The long noncoding RNA SChLAP1 promotes aggressive prostate cancer and antagonizes the SWI/SNF complex. Nat. Genet. *45*, 1392–1398.

Quinlan, A.R., and Hall, I.M. (2010). BEDTools: a flexible suite of utilities for comparing genomic features. Bioinformatics *26*, 841–842.

Ramírez, F., Dündar, F., Diehl, S., Grüning, B.A., and Manke, T. (2014). deepTools: a flexible platform for exploring deep-sequencing data. Nucleic Acids Res. *42*, W187–W191.

Ran, F.A., Hsu, P.D., Wright, J., Agarwala, V., Scott, D.A., and Zhang, F. (2013). Genome engineering using the CRISPR-Cas9 system. Nat. Protoc. *8*, 2281–2308.

Riising, E.M., Comet, I., Leblanc, B., Wu, X., Johansen, J.V., and Helin, K. (2014). Gene silencing triggers polycomb repressive complex 2 recruitment to CpG islands genome wide. Mol. Cell *55*, 347–360.

Rinn, J.L., and Chang, H.Y. (2012). Genome regulation by long noncoding RNAs. Annu. Rev. Biochem. *81*, 145–166.

Rinn, J.L., Kertesz, M., Wang, J.K., Squazzo, S.L., Xu, X., Brugmann, S.A., Goodnough, L.H., Helms, J.A., Farnham, P.J., Segal, E., and Chang, H.Y. (2007). Functional demarcation of active and silent chromatin domains in human HOX loci by noncoding RNAs. Cell *129*, 1311–1323.

Robinson, M.D., McCarthy, D.J., and Smyth, G.K. (2010). edgeR: a Bioconductor package for differential expression analysis of digital gene expression data. Bioinformatics *26*, 139–140.

Robinson, J.T., Thorvaldsdóttir, H., Winckler, W., Guttman, M., Lander, E.S., Getz, G., and Mesirov, J.P. (2011). Integrative genomics viewer. Nat. Biotechnol. *29*, 24–26.

Sarma, K., Cifuentes-Rojas, C., Ergun, A., Del Rosario, A., Jeon, Y., White, F., Sadreyev, R., and Lee, J.T. (2014). ATRX directs binding of PRC2 to Xist RNA and polycomb targets. Cell *159*, 869–883.

Schmid, M., and Jensen, T.H. (2008). The exosome: a multipurpose RNA-decay machine. Trends Biochem. Sci. *33*, 501–510.

Schmid, M., and Jensen, T.H. (2018). Controlling nuclear RNA levels. Nat. Rev. Genet. *19*, 518–529.

Schneider, C.A., Rasband, W.S., and Eliceiri, K.W. (2012). NIH Image to ImageJ: 25 years of image analysis. Nat. Methods *9*, 671–675.

Seiler, J., Breinig, M., Caudron-Herger, M., Polycarpou-Schwarz, M., Boutros, M., and Diederichs, S. (2017). The lncRNA VELUCT strongly regulates viability of lung cancer cells despite its extremely low abundance. Nucleic Acids Res. *45*, 5458–5469.

Shen, X., Liu, Y., Hsu, Y.J., Fujiwara, Y., Kim, J., Mao, X., Yuan, G.C., and Orkin, S.H. (2008). EZH1 mediates methylation on histone H3 lysine 27 and complements EZH2 in maintaining stem cell identity and executing pluripotency. Mol. Cell *32*, 491–502.

Silla, T., Karadoulama, E., Mąkosa, D., Lubas, M., and Jensen, T.H. (2018). The RNA exosome adaptor ZFC3H1 functionally competes with nuclear export activity to retain target transcripts. Cell Rep. *23*, 2199–2210.

Smith, Z.D., and Meissner, A. (2013). DNA methylation: roles in mammalian development. Nat. Rev. Genet. *14*, 204–220.

Takahashi, K., and Yamanaka, S. (2006). Induction of pluripotent stem cells from mouse embryonic and adult fibroblast cultures by defined factors. Cell *126*, 663–676.

Thorvaldsdóttir, H., Robinson, J.T., and Mesirov, J.P. (2013). Integrative Genomics Viewer (IGV): high-performance genomics data visualization and exploration. Brief. Bioinform. *14*, 178–192.

Timmers, H.T.M., and Tora, L. (2018). Transcript buffering: a balancing act between mRNA synthesis and mRNA degradation. Mol. Cell *72*, 10–17.

Wang, X., Paucek, R.D., Gooding, A.R., Brown, Z.Z., Ge, E.J., Muir, T.W., and Cech, T.R. (2017). Molecular analysis of PRC2 recruitment to DNA in chromatin and its inhibition by RNA. Nat. Struct. Mol. Biol. *24*, 1028–1038.

Wray, J., Kalkan, T., and Smith, A.G. (2010). The ground state of pluripotency. Biochem. Soc. Trans. *38*, 1027–1032.

Ying, Q.L., Wray, J., Nichols, J., Batlle-Morera, L., Doble, B., Woodgett, J., Cohen, P., and Smith, A. (2008). The ground state of embryonic stem cell self-renewal. Nature *453*, 519–523.

Young, R.A. (2011). Control of the embryonic stem cell state. Cell *144*, 940–954.

Zhang, Y., Liu, T., Meyer, C.A., Eeckhoute, J., Johnson, D.S., Bernstein, B.E., Nusbaum, C., Myers, R.M., Brown, M., Li, W., and Liu, X.S. (2008). Model-based analysis of ChIP-Seq (MACS). Genome Biol. *9*, R137.

Zhang, Q., McKenzie, N.J., Warneford-Thomson, R., Gail, E.H., Flanigan, S.F., Owen, B.M., Lauman, R., Levina, V., Garcia, B.A., Schittenhelm, R.B., et al. (2019). RNA exploits an exposed regulatory site to inhibit the enzymatic activity of PRC2. Nat. Struct. Mol. Biol. *26*, 237–247.

Zhao, J., Sun, B.K., Erwin, J.A., Song, J.J., and Lee, J.T. (2008). Polycomb proteins targeted by a short repeat RNA to the mouse X chromosome. Science *322*, 750–756.

Zhao, J., Ohsumi, T.K., Kung, J.T., Ogawa, Y., Grau, D.J., Sarma, K., Song, J.J., Kingston, R.E., Borowsky, M., and Lee, J.T. (2010). Genome-wide identification of polycomb-associated RNAs by RIP-seq. Mol. Cell *40*, 939–953.

Zhou, Q., Chipperfield, H., Melton, D.A., and Wong, W.H. (2007). A gene regulatory network in mouse embryonic stem cells. Proc. Natl. Acad. Sci. U S A *104*, 16438–16443.

## STAR★METHODS

### KEY RESOURCES TABLE

| REAGENT or RESOURCE | SOURCE | IDENTIFIER |
|---|---|---|
| Antibodies | | |
| PSRC2 (ZFC3H1) antibody | Novus Biologicals | Cat# NB100-68267; RRID:AB_2218116 |
| ZFC3H1 antibody | Sigma-Aldrich | Cat# HPA-007151; RRID:AB_1846133 |
| MTR4 (SKIV2L2) antibody | Abcam | Cat# ab70551; RRID:AB_1270701 |
| PABPN1 antibody | Abcam | Cat# ab75855; RRID:AB_1310538 |
| EXOSC4 (RRP41) antibody | In house (Pruijn lab) | Brouwer et al., 2001 |
| DIS3 antibody | Sigma-Aldrich | Cat# HPA039281; RRID:AB_10795583 |
| ZCCHC8 antibody | Abcam | Cat# ab68739; RRID:AB_1271512 |
| ACTB (β-ACTIN) antibody | Sigma-Aldrich | Cat# A2228; RRID:AB_476697 |
| NANOG antibody | Cell Signaling | Cat# 8822; RRID:AB_11217637 |
| ESRRB antibody | R+D Systems | Cat# PP-H6705-00; RRID:AB_2100412 |
| KLF2 antibody | Millipore | Cat# 09-820; RRID:AB_10807287 |
| SOX2 antibody | Santa Cruz | Cat# sc-17320; RRID:AB_2286684 |
| OCT4 antibody | Abcam | Cat# ab19857; RRID:AB_445175 |
| VCL (VINCULIN) antibody | Sigma-Aldrich | Cat# V9131; RRID:AB_477629 |
| SUZ12 antibody | Cell Signaling | Cat# 3737; RRID:AB_2196850 |
| EZH2 antibody | Cell Signaling | Cat# 5246; RRID:AB_10694683 |
| EZH2 antibody | In house (Helin lab) | AC22 |
| EZH2 antibody | Abcam | Cat# ab195409 |
| EED antibody | In house (Helin lab) | Bracken et al., 2003 |
| SFPQ antibody | Abcam | Cat# ab50935; RRID:AB_882523 |
| TUBA1B (α-TUBULIN) antibody | Rockland | Cat# 600-401-880; RRID:AB_2137000 |
| RPB1 NTD antibody | Cell Signaling | Cat# 14958; RRID:AB_2687876 |
| H3K27me3 antibody | Cell Signaling | Cat# 9733; RRID:AB_2616029 |
| H3K27ac antibody | Cell Signaling | Cat# 8173: RRID:AB_10949503 |
| H3K4me1 antibody | Cell Signaling | Cat# 5326; RRID:AB_10695148 |
| H3K4me3 antibody | Cell Signaling | Cat# 9751; RRID:AB_2616028 |
| H3 antibody | Abcam | Cat# ab1791; RRID:AB_302613 |
| H4 antibody | Millipore | Cat# 05858; RRID:AB_390138 |
| IgG | Millipore | Cat# PP64; RRID:AB_97852 |
| Bacterial and Virus Strains | | |
| DH5α Chemically Competent Cells | Prepared in lab | N/A |
| Chemicals, Peptides, and Recombinant Proteins | | |
| GSK3 inhibitor (CHIR99021) | Sigma-Aldrich | Cat# SML1046 |
| MEK1/2 inhibitor (PD0325901) | Sigma-Aldrich | Cat# PZ0162 |
| N-2 Supplement | Thermo Fisher Scientific | Cat# 17502048 |
| B-27 Supplement | Thermo-Fisher Scientific | Cat# 17504044 |
| TRIZOL Reagent | Thermo-Fisher Scientific | Cat# 15596018 |
| Lipofectamine 2000 Transfection Reagent | Thermo-Fisher Scientific | Cat# 11668019 |
| Protein A Dynabeads | Thermo-Fisher Scientific | Cat# 10008D |
| Agencourt AMPure XP Beads | Thermo-Fisher Scientific | Cat# 10136224 |
| Benzonase nuclease | Millipore | Cat# 70746 |
| RNaseA | Thermo-Fisher Scientific | EN0531 |

(*Continued on next page*)

*Continued*

| REAGENT or RESOURCE | SOURCE | IDENTIFIER |
|---|---|---|
| Critical Commercial Assays | | |
| RNeasy Mini Kit | QIAGEN | Cat# 74106 |
| Dynabeads mRNA Purification Kit | Thermo Fisher Scientific | Cat# 61006 |
| Taqman Reverse Transcription Reagents | Thermo Fisher Scientific | Cat# N8080234 |
| Truseq Stranded Total RNA Library Prep Gold Kit | Illumina | Cat# 20020598 |
| Subcellular Protein Fractionation Kit for Cultured Cells | Thermo Fisher Scientific | Cat# 78840 |
| NEBNext Ultra II DNA Library Prep Kit for Illumina | NEB | Cat# E7645S |
| Deposited Data | | |
| *Ezh1*$^{-/-}$/*Ezh2*$^{-/-}$ RNA-seq data | Gene Expression Omnibus (GEO) | GSE103685 |
| Deposited RNA-seq, ChIP-seq, RIP-seq datasets | This study | GSE137491 |
| Experimental Models: Cell Lines | | |
| ES-E14TG2a cell line | ATCC | N/A |
| ES-E14TG2a *Zfc3h1*$^{-/-}$ #1 | This study | N/A |
| ES-E14TG2a *Zfc3h1*$^{-/-}$ #2 | This study | N/A |
| ES-E14TG2a *Zfc3h1*$^{-/-}$ #3 | This study | N/A |
| Oligonucleotides | | |
| sgRNA primers | See Table S1 | N/A |
| qRT-PCR primers | See Table S2 | N/A |
| Software and Algorithms | | |
| ImageJ (1.51h) | NIH, Univ. of Wisc. Madison | https://imagej.nih.gov/ij/ |
| IGV (2.4.14) | Robinson et al., 2011 | https://software.broadinstitute.org/software/igv/ |
| cellSens Entry (1.16) | Olympus | https://www.olympus-lifescience.com/en/software/cellsens/ |
| Graphpad Prism (7.0a) | Graphpad | https://www.graphpad.com/scientific-software/prism/ |
| HISAT (0.1.6.beta) | Kim et al., 2015 | http://www.ccb.jhu.edu/software/hisat/index.shtml |
| bedtools (2.23.0) | Quinlan and Hall., 2010 | https://bedtools.readthedocs.io/en/latest/ |
| Rsubread (1.32.1) | Liao et al., 2013 | https://bioconductor.org/packages/release/bioc/html/Rsubread.html |
| edgeR (3.24.1) | Robinson et al., 2010 | https://bioconductor.org/packages/release/bioc/html/edgeR.html |
| Trim Galore (0.4.4) | Babraham Institute | https://www.bioinformatics.babraham.ac.uk/projects/trim_galore/ |
| EaSeq (1.111) | Lerdrup et al., 2016 | https://easeq.net/ |
| SAMtools (1.6.1) | Li et al., 2009 | http://samtools.sourceforge.net/ |
| deepTools (2.5.3) | Ramírez et al., 2014 | https://deeptools.readthedocs.io/en/develop/ |
| Bowtie | Langmead and Salzberg., 2012 | http://bowtie-bio.sourceforge.net/index.shtml |
| MACS2 (2.1.1.20160309) | Zhang et al., 2008 | https://github.com/taoliu/MACS/ |

## LEAD CONTACT AND MATERIALS AVAILABILITY

Further information and requests for resources and reagents should be directed to and will be fulfilled by the Lead Contact, Torben Heick Jensen (thj@mbg.au.dk).

All unique/stable reagents generated in this study are available from the lead contact upon request.

## EXPERIMENTAL MODEL AND SUBJECT DETAILS

### mES cell culture and differentiation

E14TG2a mouse ESCs (male genotype, XY) were cultured on 0.2% gelatin coated plates in 2i/LIF containing medium (1:1 mix of Neurobasal (GIBCO) and DMEM/F-12 (GIBCO) supplemented with 1x Pen-Strep (GIBCO), 2 mM Glutamax (GIBCO), 50 μM

β-mercaptoethanol (GIBCO), 0.1 mM nonessential amino acids (GIBCO), 1 mM sodium pyruvate (GIBCO), 0.5x N2 supplement (GIBCO), 0.5x B27 supplement (GIBCO), 3 μM GSK3i (CHIR99021), 1 μM MEKi (PD0325901) and Leukemia Inhibitory Factor (LIF; produced in house)). Cells were passaged every 2-3 days by aspirating medium, dissociating cells with 0.25% trypsin-EDTA (GIBCO) briefly at 37°C before the addition of an equal volume of 1x trypsin inhibitor (Sigma) and gentle disruption by pipetting. Cells were pelleted by centrifugation, washed in 2i-LIF to remove excess trypsin and pelleted again before resuspending and plating ~1x10$^6$ cells/10 cm plate.

For differentiation into EBs, dissociated cells were washed 2x in Serum-LIF (GMEM (Sigma) supplemented with 10% heat-inactivated fetal bovine serum, 1x Pen-Strep (GIBCO), 2 mM Glutamax (GIBCO), 0.1 mM nonessential amino acids (GIBCO), 1 mM sodium pyruvate (GIBCO), 50 μM β-mercaptoethanol (GIBCO)) before seeding 1.5x10$^6$ cells into 10 cm Petri-dishes containing Serum-LIF media. Media was changed at days 2, 3, 5 and 7. At day 7, EBs were transferred to 0.2% gelatin coated plates and grown for a further 3 days.

Phase contrast microscopy images were captured using an Olympus IX73 inverted microscope using the cellSens Entry software (Olympus).

## METHOD DETAILS

### CRISPR/Cas9 KOs

KO cell lines were generated by CRISPR/Cas9 targeting of *Zfc3h1* in WT ESC. Single guide (sg) RNAs (Table S1) were cloned into the pSPCas9(BB)-2A-GFP vector (pX458, Addgene plasmid ID: 48138) as previously described (Ran et al., 2013) and transfected into ES cells using Lipofectamine 2000 (Thermo). Single cell clones were isolated by GFP sorting using FACS into 0.2% gelatin coated 96 well plates containing 2i/LIF and expanded. KO clones were screened by western blotting analysis and validated by Sanger sequencing of amplified genomic DNA around the cut site. Three independent *Zfc3h1*$^{-/-}$ cell lines were derived from expanded single cell clones.

### RNA isolation

Total RNA was isolated using the RNeasy Mini Kit (QIAGEN) according to the manufacturer's instructions or by Trizol extraction (Thermo) using the standard protocol. For chromatin associated RNA, samples were prepared as previous described (Conrad and Ørom, 2017).

### pA$^+$ RNA purification

pA$^+$ RNA was isolated from nuclear RNA samples using the Dynabeads mRNA Purification Kit (Thermo). For isolation of nuclei, 2x10$^7$ cells were resuspended in nuclear isolation buffer (NIB) (10 mM Tris pH 7.4, 150 mM NaCl, 0.15% Igepal CA-630) supplemented with protease inhibitors and lysed at 4°C on a rotating wheel for 5 minutes. Lysates were overlaid onto 1 mL Sucrose buffer (10 mM Tris pH 7.4, 150 mM NaCl, 24% sucrose) in a DNA LoBind tube (Eppendorf) and nuclei were pelleted for 10 minutes at 2000 x g. Nuclei were resuspended in 1 mL Trizol (Thermo) and RNA was extracted using the standard protocol. 50 μg of nuclear RNA extracts were heated to 65°C and cooled on ice before incubating with oligo dT(25) Dynabeads (Thermo). Bead complexes were washed twice before elution in 10 mM Tris pH 7.5 and recovered RNA were assessed using a NanoDrop Lite Spectrophotometer (Thermo).

### qRT-PCR analysis

cDNA was prepared from 500 ng of total RNA with TaqMan Reverse Transcription reagents (Thermo) using random hexamers. qRT-PCR was performed using the LightCycler 480 SYBR Green I (Roche) in technical triplicates. Primers used in qRT-PCR are listed in Table S2.

### RNA-seq library preparation

RNA-seq libraries were prepared from 1 μg of total RNA using the TruSeq Stranded Total RNA library prep kit with RiboZero Gold (Illumina) according to the manufacturer's instructions. Three biological replicates from each sample were prepared. RNA integrity and library quality were assessed on a Bioanalyzer 2000 using RNA Nano and DNA 1000 chips (Agilent), respectively. Libraries were quantified and normalized for multiplexing using the KAPA library quantification Kit for Illumina (KAPA Biosystems) and sequenced on an Illumina NextSeq 550 (75-bp, paired-end).

### Western blotting analysis

Protein lysates were prepared using TOPEX+ buffer (Riising et al., 2014) (300 mM NaCl, 50 mM Tris-HCl pH 7.5, 0.5% Triton X-100, 1% SDS) freshly supplemented with protease inhibitors, 1 mM DTT and 33.3 U/ml Benzonase (Novagen). SDS-PAGE and western blotting analysis were carried out according to standard protocols with the antibodies listed in the Key Resources Table and HRP conjugated secondary antibodies (Vector Laboratories and Agilent). Bands were visualized by Super Signal West Pico chemiluminescent ECL (Thermo) and exposed either on Amersham Hyperfilm ECL films (GE Healthcare) and developed (Ferrania Imagine Technologies) or digitally captured using an Amersham Imager 600 (GE Healthcare). Images were processed and quantified using ImageJ (Schneider et al., 2012).

### IP experiments

For whole cell IPs, 1x10$^7$ cells/IP were resuspended in HT150 extraction buffer (20 mM HEPES pH 7.4, 150 mM NaCl, 0.5% Triton X-100) supplemented with protease inhibitors and sheared mechanically using 22 G and 27 G needles sequentially with 6 strokes each. For nuclear IPs, 1x10$^7$ cells/IP were resuspended in nuclear isolation buffer (NIB) (10 mM Tris pH 7.4, 150 mM NaCl, 0.15% Igepal CA-630) supplemented with protease inhibitors and lysed at 4°C on a rotating wheel for 5 minutes. Lysates were overlaid onto 1 mL Sucrose buffer (10 mM Tris pH 7.4, 150 mM NaCl, 24% sucrose) in a DNA LoBind tube (Eppendorf) and nuclei were pelleted for 10 minutes at 2000 x g. Nuclei were resuspended in 250 μl/IP RNA isolation buffer (RIB) (25 mM Tris pH 7.4, 150 mM KCl, 0.5 mM DTT, 0.5% Igepal CA-630) supplemented with protease inhibitors and sheared mechanically using 22 G and 27 G needles sequentially with 6 strokes each.

Clarified lysates were treated with DNaseI (Thermo) for 20 minutes at 37°C before pre-clearing with rabbit IgG (Millipore) and Protein-A Dynabeads (Thermo) for 2 hours at 4°C. Supernatants were incubated with either IgG, SUZ12 (Cell Signaling) or EZH2 (made in house) antibodies overnight at 4°C with Protein-A Dynabeads. Beads were washed 3 times with the respective extraction buffer, transferring beads to a fresh tube on the final wash. Proteins were eluted by boiling in 1X NuPAGE loading buffer (Invitrogen). 10X reducing agent (Invitrogen) was added to the supernatants before denaturing for 10 minutes at 95°C and proceeding with western blotting analysis.

### Glycerol gradient sedimentation analysis

The glycerol gradient sedimentation analysis was performed as previously described (Chu et al., 2014), with minor modifications. Briefly, whole cell extracts from ~2x10$^8$ cells were resuspended in BC100 buffer (5 mM HEPES pH 7.5, 100 mM NaCL, 1 mM $MgCl_2$, 0.5 mM EGTA, 0.1 mM EDTA, 10% v/v glycerol, 1 mM DTT) supplemented with protease inhibitors, lysed by sonication (3 × 5 s, amplitude 2) and centrifuged at 14,000 rpm for 20 minutes. Clarified lysates were loaded on 10%–50% (v/v) glycerol gradients prepared in BC100 buffer and centrifuged at 35,000 rpm for 28 hours using a SW41 rotor (Beckman). Gradients were separated into 18 fractions and protein content was assessed using the Bradford assay (Bio-Rad). Remaining fractions were TCA precipitated, acetone washed and resuspended in 1x NuPAGE loading buffer (Thermo). Samples were separated by SDS-PAGE and analyzed either by western blotting analysis or using the Blue Silver modified Neuhoff's colloidal Coomassie Blue G-250 stain (Candiano et al., 2004).

### RNaseA treatment

Cells were treated with RNaseA as previously described (Beltran et al., 2016). Cells were trypsinised and permeabilised with 0.05% Tween-20 (Sigma) in PBS for 10 minutes on ice. Cells were washed once, resuspended in PBS and either mock-treated or treated with 1 mg ml$^{-1}$ RNaseA (Thermo) for 30 minutes at RT with gentle agitation. Cells were washed twice with PBS before proceeding with lysis and IP.

### Subcellular fractionation

Cells were separated into cytoplasmic, nuclear and chromatin fractions using the Subcellular Protein Fractionation Kit (Pierce) according to the manufacturer's instructions. Cells were harvested in 1x10$^7$ aliquots, split into 2 samples for either whole cell extraction using TOPEX+ buffer or fractionation. Equivalent lysate volumes were separated by SDS-PAGE and analyzed by western blotting.

### RIP experiments

Whole cell IPs were performed as described above with alterations. All buffers were additionally supplemented with 100 U/ml RiboLock RNase Inhibitor (Thermo). Following overnight IP with IgG, SUZ12 or EZH2 antibodies, beads were washed 3 times with HT150 buffer, transferring beads to a fresh tube on the final wash. RNA was isolated from the IPs by the addition of 1 mL Trizol, homogenization and incubating for 1 hour on ice. Beads were removed magnetically and RNA was isolated from Trizol using the standard protocol.

### RIP-seq

Strand specific libraries were prepared from ~200 ng RNA isolated in SUZ12 and EZH2 RIP experiments by BGI Tech Solutions (Europe) according to their lncRNA-seq library preparation protocol. Two biological replicates were prepared from each sample. RNA integrity was assessed using a BioAnalyzer 2000 (Agilent) using RNA Nano chips. Samples were ribodepleted using Ribo-Zero (Illumina) and libraries prepared using the TruSeq Stranded mRNA library prep kit (Illumina). Libraries were sequenced on a BGISEQ-500 (100 bp, paired end).

### ChIP experiments

ChIP experiments were carried out according to standard protocols. Briefly, ES cells were cross-linked by the addition of 1% formaldehyde (Sigma) in the dish for 10 minutes at RT before quenching with glycine. DNA was sheared to ~200 bp fragments by sonication using a Biorupter (Diagenode) and validated by agarose gel electrophoresis. ChIPs were carried out using 200 μg of chromatin and 2-3 μg of the indicated antibodies (Key Resources Table). Libraries for ChIP-seq were prepared using NEBNext Ultra II DNA Library prep kit (NEB) using AmpureXP beads (Beckman) for size selection. Libraries were assessed on a Bioanalyzer 2000 (Agilent)

using High Sensitivity DNA chips and quantified using the Qubit dsDNA HS assay kit (Thermo). Libraries were sequencing on an Illumina NextSeq 550 (75 bp, single end).

## QUANTIFICATION AND STATISTICAL ANALYSIS

### Processing and analysis of RNA-seq data

Quality control of sequence reads was done using FastQC v0.11.2 (http://www.bioinformatics.babraham.ac.uk/projects/fastqc/). Illumina adaptors (as provided with the FastQC tool), low quality bases, the first 12 bases and reads shorter than 25 nt were removed with Trimmomatic v0.32, using settings "ILLUMINACLIP:<TrueSeq3_PE_2>:2:30:10 HEADCROP:12 LEADING:22 SLIDING WINDOW:4:22 MINLEN:25" (Bolger et al., 2014). Both paired and unpaired (due to the trimming) reads were mapped using HISAT v0.1.6.beta (Kim et al., 2015), against the mouse genome (mm10), where a list of GENCODE M12 (Frankish et al., 2019) annotated splice sites was also provided. HISAT was furthermore run with maximum fragment length set to 1000 and the–rf parameter (for the upstream/downstream mate orientation), otherwise default settings was used.

To generate visualization, properly paired reads mapping onto unique genomic locations were selected. Genomecov from bedtools v2.23.0 (Quinlan and Hall, 2010) was used to calculate strand-specific per-base genome coverage in bedgraph format. Bedgraph files were converted into bigwig format for using the UCSC Genome Browser Utility 'bedGraphToBigWig' (Kent et al., 2010). Finally, the per base coverage was CPM normalized. Genome browser images are generated from IGV (Robinson et al., 2011; Thorvaldsdóttir et al., 2013)

Paired and uniquely mapped exonic reads for GENCODE M12 genes were counted using featureCounts from the R package Rsubread (1.32.1) (Liao et al., 2013) for individual RNA-seq libraries. RNA-seq read counts for PRC2 KO (*Ezh1*$^{-/-}$/*Ezh2*$^{-/-}$) and corresponding WT samples were obtained from the Gene Expression Omnibus (GEO), accession number: GSE103685 (Højfeldt et al., 2018). Differential expression analysis was performed using the R package edgeR (version 3.24.1) with default parameters (McCarthy et al., 2012; Robinson et al., 2010). Intronic regions of a gene were defined as regions in the gene body that do not overlap with an exon from any GENCODE M12 annotated transcript isoform. Intronic reads were counted and differential expression analysis was performed using the same method as for exonic reads.

### Processing and analysis of RIP-seq data

Quality control of sequence reads was done using FastQC v0.11.2. Illumina adaptors, low-quality bases with Phred score lower than 20, and reads shorter than 25 bp were removed using Trim Galore (version: 0.4.4, https://www.bioinformatics.babraham.ac.uk/projects/trim_galore/); reads were further trimmed using parameters–clip_R1 13–clip_R2 13–three_prime_clip_R1 1–three_prime_clip_R2 1. Trimmed reads were mapped as described for RNA-seq data processing. BAM alignment files were further processed to select uniquely mapped and properly paired reads using SAMtools (version 1.6.1) (Li et al., 2009). Duplicated reads were removed using MarkDuplicates (version: 2.8.1) from GATK (McKenna et al., 2010) with default settings and processed BAM files were used for downstream analysis. The strand specific genomic coverage was calculated using bamCoverage from deepTools (Ramírez et al., 2014). Raw reads for GENCODE M12 genes were counted using the same method as for RNA-seq, and differential analysis was performed using edgeR. To calculate the enrichment of transcripts pulled down by SUZ12 and EZH2 IPs in *Zfc3h1*$^{-/-}$ compared to WT, contrast in the differential analysis was made as (*Zfc3h1*$^{-/-}$ IP – *Zfc3h1*$^{-/-}$ input) – (WT IP – WT input) and the enrichment score was defined as log2 fold change calculated from the contrast.

### Processing and analysis of ChIP-seq data

Reads were mapped onto the mouse (mm10) genome with Bowtie (Langmead and Salzberg, 2012), selecting only hits with the best stratum with up to two mismatches in the seed and reporting up to four good alignments per read. Only two copies of identical reads were kept. The fragment sizes could be deduced using the ChIP-Cor tool (Ambrosini et al., 2016). Reads were shifted to the center of their fragment by half of the deduced fragment size. Genomecov from bedtools v2.23.0 (Quinlan and Hall, 2010) was used to calculate strand specific per base genome coverage in bedgraph format. Bedgraph files were converted into bigwig format for using the UCSC Genome Browser Utility 'bedGraphToBigWig' (Kent et al., 2010). Finally, the per base coverage was CPM normalized.

For global MA plots, ChIP signals from all libraries were quantified on genomic windows of 2 kb sliding by 500 bp using the UCSC Genome Browser Utility 'bigWigAverageOverBed' (Kent et al., 2010). SUZ12 peaks were called using MACS2 (Zhang et al., 2008) (version 2.1.1.20160309) with parameters–qvalue 0.05–broad–broad-cutoff 0.3, ENCODE blacklisted peaks (ENCODE Project Consortium, 2012) and low quality peaks (-$\log_{10}$(qvalue) $\leq$ 1) were filtered out. Consistent SUZ12 peaks between *Zfc3h1*$^{-/-}$ replicates were defined as peaks overlapping in at least two replicates. A single SUZ12 reference peak set for WT and *Zfc3h1*$^{-/-}$ was obtained by pooling SUZ12 peaks of WT and consistent SUZ12 peaks of *Zfc3h1*$^{-/-}$ and merging overlapping peak regions into a single region using mergeBed from bedtools (v2.23.0). Raw reads of H3K27me3 and SUZ12, for SUZ12 peaks in the reference peak set, were obtained using featureCounts from the R package Rsubread (1.32.1), a pseudocount of 1 was added when normalizing raw read counts to the library size. $\log_2$FC values were calculated between mean values of the normalized read counts from *Zfc3h1*$^{-/-}$ replicates and the normalized read counts from WT. For mean signal plots, genomic coverage from bigWig files was calculated using computeMatrix from deepTools (version 2.5.3) (Ramírez et al., 2014). Regions without read coverage in bigWig files were treated as 0, mean values from the replicates were calculated and mean values at each position were plotted. For the heatmap, a list of genes

overlapping with at least one SUZ12 peak from the reference peak set was obtained, H3K27me3 and SUZ12 were quantified in the gene bodies, $log_2$FC values of H3K27me3 and SUZ12 between *Zfc3h1*$^{-/-}$ and WT were calculated using the method described above, and $log_2$FC values of gene exonic expression were computed from the differential expression analysis of RNA-seq described above.

## DATA AND CODE AVAILABILITY

All high-throughput RNA-seq, ChIP-seq and RIP-seq datasets generated during this study are available at the Gene Expression Omnibus (GEO) under accession code GSE137491.